Monthly Notices
of the
ROYAL ASTRONOMICAL SOCIETY

MNRAS **456,** 1803–1825 (2016) doi:10.1093/mnras/stv2723

s-process production in rotating massive stars at solar and low metallicities

Urs Frischknecht,[1,2] Raphael Hirschi,[1,3,4⋆] Marco Pignatari,[5] André Maeder,[6] George Meynet,[6] Cristina Chiappini,[7] Friedrich-Karl Thielemann,[2] Thomas Rauscher,[2,4,8] Cyril Georgy[1] and Sylvia Ekström[6]

[1]*Astrophysics group, Lennard-Jones Laboratories, Keele University, Staffordshire ST5 5BG, UK*
[2]*Department of Physics, University of Basel, Klingelbergstr. 82, CH-4056 Basel, Switzerland*
[3]*Kavli Institute for the Physics and Mathematics of the Universe (WPI), University of Tokyo, 5-1-5 Kashiwanoha, Kashiwa, Chiba 277-8583, Japan*
[4]*UK Network for Bridging Disciplines of Galactic Chemical Evolution (BRIDGCE), http://www.bridgce.net/, UK*
[5]*Konkoly Observatory, Hungarian Academy of Sciences, Konkoly Thege Miklos ut 15-17, H-1121 Budapest, Hungary*
[6]*Geneva Observatory, Geneva University, CH-1290 Sauverny, Switzerland*
[7]*Leibniz-Institut für Astrophysik Potsdam (AIP), An der Sternwarte 16, D-14482 Potsdam, Germany*
[8]*Centre for Astrophysics Research, School of Physics, Astronomy and Mathematics, University of Hertfordshire, Hatfield AL10 9AB, UK*

Accepted 2015 November 18. Received 2015 November 17; in original form 2015 July 29

ABSTRACT

Rotation was shown to have a strong impact on the structure and light element nucleosynthesis in massive stars. In particular, models including rotation can reproduce the primary nitrogen observed in halo extremely metal poor (EMP) stars. Additional exploratory models showed that rotation may enhance *s*-process production at low metallicity. Here we present a large grid of massive star models including rotation and a full *s*-process network to study the impact of rotation on the weak *s*-process. We explore the possibility of producing significant amounts of elements beyond the strontium peak, which is where the weak *s*-process usually stops. We used the Geneva stellar evolution code coupled to an enlarged reaction network with 737 nuclear species up to bismuth to calculate 15–40 $M_\odot$ models at four metallicities ($Z = 0.014$, 10^{-3}, 10^{-5} and 10^{-7}) from the main sequence up to the end of oxygen burning. We confirm that rotation-induced mixing between the convective H-shell and He-core enables an important production of primary ^{14}N and ^{22}Ne and *s*-process at low metallicity. At low metallicity, even though the production is still limited by the initial number of iron seeds, rotation enhances the *s*-process production, even for isotopes heavier than strontium, by increasing the neutron-to-seed ratio. The increase in this ratio is a direct consequence of the primary production of ^{22}Ne. Despite nuclear uncertainties affecting the *s*-process production and stellar uncertainties affecting the rotation-induced mixing, our results show a robust production of *s*-process at low metallicity when rotation is taken into account. Considering models with a distribution of initial rotation rates enables us to reproduce the observed large range of the [Sr/Ba] ratios in (carbon-enhanced and normal) EMP stars.

Key words: stars: abundances – stars: chemically peculiar – stars: massive – stars: Population II – stars: rotation – Galaxy: abundances.

1 INTRODUCTION

The classic view of the *s*-process nucleosynthesis in massive stars is that it occurs in He- and C-burning regions of the stars, producing only the low-mass range of the *s*-process elements, typically the elements with an atomic mass number below about 90–100 (e.g. Käppeler et al. 2011, and references therein). It has also been shown that in the regions where the *s*-process occurs, the fact that, when the metallicity decreases, (1) the neutron source, mainly the ^{22}Ne(α, n) reaction, decreases, (2) the neutron seeds (Fe) also decrease, (3) the neutron poisons as for instance ^{16}O remain independent of the metallicity implies that the *s*-process element production decreases with the metallicity and that there exists some limiting

⋆ E-mail: r.hirschi@keele.ac.uk

metallicity below which the *s*-process becomes negligible. This limit was found to be around $Z/Z_{\odot} = 10^{-2}$ (Prantzos, Hashimoto & Nomoto 1990).

First attempts to investigate the possible role of rotational mixing on the *s*-process production in massive stars have shown that this classic picture could be significantly revised. The impact of rotation on the *s*-process nucleosynthesis in low-*Z* massive rotating stars was studied by Pignatari et al. (2008). In that study, the *s*-process production was investigated by assuming different concentrations of primary ^{22}Ne in the convective He-burning core, guided by the early results of Hirschi (2007). Frischknecht, Hirschi & Thielemann (2012) presented 25 $M_{\odot}$ stellar models at various metallicities and with different initial rotation rates using an *s*-process network of 612 isotopes up to the end of core He-burning and 737 isotopes during the later stages. The main results of these works were that the *s*-process production could be boosted in models with strong rotational mixing, that isotopes with an atomic mass heavier than 100 can be synthesized and that very different ratios of first to second peak *s*-process element ratios can be obtained depending on the rotation rate.

The main reason for these changes comes from the following process: rotational mixing allows the production of large amounts of ^{14}N in the H-burning shell, ^{14}N, which, once engulfed into the He-burning core, is transformed into ^{22}Ne via two α-captures. Increasing the quantity of ^{22}Ne favours *s*-process production since the main neutron source is the ^{22}Ne(α,n) reaction. Nevertheless, the limiting factors mentioned just above at low metallicity, namely the decrease of the seeds while the amount of important neutron poisons does not change, remain whatever the star is rotating or not. Thus, rotation acts mainly on one of the aspect of the *s*-process nucleosynthesis, the neutron source via the amount of ^{22}Ne, leaving the other more or less the same as in the non-rotating models. Rotation can also have an impact on the *s*-process through its influence on the size of the H- and He-burning cores, but these effects remain modest compared to the impact linked to the ^{22}Ne.

While the above-mentioned studies provide already the general trends of how rotation will impact the *s*-process production, they focus on only one initial mass. In the present work, we extend the mass range explored. In that respect, this is the first extended grid of this kind that is published and we hope that this will trigger new theoretical predictions in the future exploring other physics, such as the impact of an internal magnetic field or of the presence of a close binary companion.

Before entering into the main body of this paper, we would like to emphasize an additional point, the fact that rotation has a particularly strong impact at low metallicity, and therefore on the evolution and nucleosynthesis of the first stellar generations in the Universe.

Due to their low metal content, they are more compact and rotate faster than their equivalents found in the Milky Way. This view is supported by observations of an increasing Be/B-type star ratio with decreasing metallicity (Martayan et al. 2007) and by faster rotating massive stars in the Small Magellanic Cloud (SMC) compared to the Milky Way (Hunter et al. 2008).

Fast-rotating stellar models at low *Z* have been calculated by Meynet, Ekström & Maeder (2006) and Hirschi (2007). In these models, nitrogen yields are much larger than in non-rotating models. When yields from these rotating models are used as input in chemical evolution models, a nice fit of the N/O in very metal poor halo stars (see e.g. Spite et al. 2005) can be obtained (Chiappini et al. 2006). The nitrogen production in rotating low-*Z* stellar models is accompanied by large production of other isotopes like ^{13}C, and especially ^{22}Ne, which is, as recalled above, the neutron source for *s*-process in massive stars (e.g. Käppeler et al. 2011, and references therein).

The observation of large *s*-process enhancements in one of the oldest globular clusters in the bulge of our Galaxy supports the view that massive stars could indeed be also important sources for these elements (Chiappini et al. 2011), highlighting the need for comprehensive calculations of *s*-process in low-*Z* massive rotating stars. This motivated us to produce a large grid of low-*Z* massive rotating star models including a full *s*-process network. The observations by Barbuy et al. (2009) and Chiappini et al. (2011) were later updated by Barbuy et al. (2014) and Ness, Asplund & Casey (2014). In particular, Barbuy et al. (2014) confirmed that at least part of the stars in the globular cluster NGC 6522 is compatible with the *s*-process production in fast-rotating massive stars at low metallicity. Galactic chemical evolution (GCE) models using the larger grid of models were presented in Cescutti et al. (2013, 2015, with some modifications explained in these papers) and showed that rotation-induced mixing is able to explain the large scatter for [Sr/Ba] observed in extremely metal poor stars. In this paper, we present the large grid of low-*Z* massive rotating star models including a full *s*-process network used in the GCE models listed above.

We describe our models in Section 2. The mixing induced by rotation and the production of primary ^{22}Ne are discussed in Section 3. We revisit the *s*-process in non-rotating stars and its dependence on initial metallicity in Section 3. The impact of rotation on the *s*-process in massive stars at different metallicities is discussed in Section 5. We compare our models to the literature and observations in Section 6. Finally, we give our conclusions in Section 7.

2 MODELS AND YIELD CALCULATIONS

2.1 Model ingredients

We calculated the stellar evolution models with the Geneva stellar evolution code (GENEC), which is described in detail in Eggenberger et al. (2008). The main improvement brought to GENEC for these models is the integration of a large nuclear reaction network (613 isotopes up to the end of He-burning and 737 from thereon). The smaller network is almost identical to the *s*-process network used by The, El Eid & Meyer (2000, see their table 1). This version of GENEC with an enhanced nucleosynthesis network size and the nucleosynthesis network coupled to the structure is the same as in Frischknecht et al. (2012) and The et al. (2000). Since rotation-induced mixing is of prime importance in this work, we briefly review here the input physics used. We used the horizontal diffusion coefficient of Zahn (1992) and the shear diffusion coefficient from Talon & Zahn (1997), which is a conservative choice since this prescription includes a strong reduction of mixing across mean molecular weight gradients.

In the reaction library used for the network calculations, theoretical neutron capture and charged particle rates from Rauscher & Thielemann (2000) were used unless experimental information was available as outlined below. The charged particle reaction rates from Angulo, Arnould & Rayet (NACRE compilation, 1999) were used except for the following reactions: ^{22}Ne(α,n) and the 3α-rate were taken from Jaeger et al. (2001) and from Fynbo et al. (2005), respectively. Neutron capture rates present in the KADoNiS compilation (v0.1; Dillmann et al. 2006) were implemented. Beta-decay rates derived from experimental beta-decay half-lives were used except for

the temperature-dependent rates given in Takahashi & Yokoi (1987). The REACLIB parameters for 3α, ^{12}C(α, γ)^{16}O, ^{14}N(p, γ)^{15}O and the constant beta-decay rates beyond Pd were obtained from the JINA-REACLIB website (groups.nscl.msu.edu/jina/reaclib/db). Two of the most important nuclear reaction rates for *s*-process in massive stars are ^{22}Ne(α, n) and ^{22}Ne(α, γ). The rates used in this study, taken from Jaeger et al. (2001) and NACRE, respectively, result in an equal strength of both channels at $T \approx 2.8 \times 10^8$ K ($T_8 \approx 2.8$). Below this temperature, the (α, γ) channel dominates, while above the (α, n) channel is stronger. In our models, an important fraction of ^{22}Ne is burned when ^{22}Ne(α, γ) dominates over the neutron source. More recent rate determinations of ^{22}Ne(α, γ) from Karakas et al. (2006) or Iliadis et al. (2010), Longland, Iliadis & Karakas (2012) and Bisterzo et al. (2015) are not used in this work, but are all lower than the NACRE rate. This means that the yields from He-core burning could be higher, depending also on the ratio between the (α, n) and (α, γ) channels. Previous impact studies of the ^{22}Ne(α, γ) and ^{22}Ne(α, n) rates on the *s*-process in massive stars are e.g. Käppeler et al. (1994), Rauscher et al. (2002), Pignatari et al. (2010) and Nishimura et al. (2014).

In the stellar models presented in this work, for ^{17}O(α, γ) and ^{17}O(α, n) reaction rates we used the rates of Caughlan & Fowler (1988, hereafter CF88) and Angulo et al. (1999), respectively. Their ratio determines the strength of ^{16}O as a neutron poison (e.g. Baraffe, El Eid & Prantzos 1992; Hirschi et al. 2008). Descouvemont (1993) predicted that the ^{17}O(α, γ) should be a factor of 1000 smaller than the CF88 rate. More recently, two independent groups measured the ^{17}O(α, γ) rate (Best et al. 2011, 2013; Taggart, Hager & Laird 2011), obtaining a rate lower than CF88 at relevant temperatures, but not as low as Descouvemont (1993). Best et al. (2013) also provided a new rate for the ^{17}O(α, n). In order to assess the impact of a lower ^{17}O(α, γ) rate, we calculated the rotating 25 $M_\odot$ models at $Z = 10^{-5}$ (C25s4, C25s5) and 10^{-7} (D25s4, D25s6) with the CF88 rate divided by a factor 10, which is consistent with the new measurements within the uncertainties. These models are in the following text labelled by an additional 'b' at the end of their name. Although the 25 $M_\odot$ models have already been discussed in Frischknecht et al. (2012), we provide more details about these models in this paper, and it is important to present models of all masses in a single paper.

The mass range from 15 and 40 $M_\odot$ was investigated, with models of 15, 20, 25 and 40 $M_\odot$ and for each mass a model without rotation and at least one with rotation were calculated. The stellar models were calculated from zero-age main-sequence (ZAMS) up to O-burning for the grid of models, which is shown in Table 1. Models with masses below 15 $M_\odot$ were not followed, because the temperature is not high enough to efficiently activate the neutron source. The observed *s*-process nuclei are usually also not considered to originate from stars beyond 40 $M_\odot$, because more massive stars are thought to collapse directly to black holes at the end of their life without an explosion, while stars between 25 and 40 $M_\odot$ lead to black hole formation by matter falling back on the remnant neutron star (e.g. Woosley, Heger & Weaver 2002; Heger et al. 2003). In the latter case, an explosion still happens, ejecting fractions of the synthesized elements. Let us note, however, that the above mass limits between the different scenarios for the ultimate explosion are very uncertain and depend on many factors such as the metallicity and the input physics used in the stellar modelling (see the recent review by Janka 2012, and references therein). All masses were calculated at initial metallicities, $Z = 0.014$ (solar metallicity models, starting with letter A), 10^{-3} (B) and 10^{-5} (C), to investigate the metallicity dependence of the *s*-process in massive rotating stars. Additionally, 25 $M_\odot$ stars at $Z = 10^{-7}$ were modelled. The [Fe/H] values corresponding to these four metallicities are 0, −1.8, −3.8 and −5.8. For $Z = 0.014$, we have adopted the elemental composition of Asplund, Grevesse & Sauval (2005), with the modified Ne abundance of Cunha, Hubeny & Lanz (2006), and the isotopic ratios from Lodders (2003). At all three sub-solar metallicities, we assumed an α-enhanced composition with the α-elements (^{12}C, ^{16}O, ^{20}Ne, ^{24}Mg, ^{28}Si, ^{32}S, ^{36}Ar, ^{40}Ca and ^{48}Ti) enhanced with respect to iron, i.e. $[X/\mathrm{Fe}] = -A[\mathrm{Fe/H}]$ for $-1 \geq [\mathrm{Fe/H}] > 0$ and $[X/\mathrm{Fe}] = A =$ constant for $[\mathrm{Fe/H}] \leq -1$ where $A = +0.562, +0.886, +0.500, +0.411, +0.307, +0.435, +0.300, +0.222$ and $+0.251$ for the different α-enhanced isotopes. This α-enhanced composition was derived by fitting the abundance trends [*X*/Fe] versus [Fe/H] derived from halo and thick disc F- and G-dwarfs (Reddy, Lambert & Allende Prieto 2006) between [Fe/H] = 0 and −1. The linear fits were fixed to the solar value, i.e. [*X*/Fe] = 0 at [Fe/H] = 0, and below [Fe/H] = −1 a plateau was assumed. The values for the noble gases were adopted from the GCE models of Kobayashi et al. (2006). This α-enhancement gives an Fe/*Z* ratio for [Fe/H] ≤ −1, which is a factor of 4.6 lower than at solar *Z*. All other elements were scaled from the solar composition.

As standard initial rotation rate 40 per cent of critical velocity ($\upsilon_{\rm ini}/\upsilon_{\rm crit} = 0.4$) was used. For 15–25 $M_\odot$ stars at solar *Z*, it corresponds to an average equatorial rotation velocity on the main

Table 1. Model parameters: initial mass (column 1), model label (2), initial ratio of surface velocity to critical velocity (3), time-averaged surface velocity during the MS phase (4), metallicity (5), [Fe/H] (6) and total lifetime, τ, from the ZAMS until the advanced phases (7).

Mass ($M_\odot$)	Model	$\frac{\upsilon_{\rm ini}}{\upsilon_{\rm crit}}$	$\langle\upsilon\rangle_{\rm MS}$ (km s^{-1})	Z	[Fe/H]	τ (Myr)
15	A15s0	0.0	0	0.014	0.0	12.7
	A15s4	0.4	200	0.014	0.0	15.0
	B15s0	0.0	0	10^{-3}	−1.8	13.1
	B15s4	0.4	234	10^{-3}	−1.8	15.4
	C15s0	0.0	0	10^{-5}	−3.8	12.9
	C15s4	0.4	277	10^{-5}	−3.8	15.0
20	A20s0	0.0	0	0.014	0.0	8.87
	A20s4	0.4	216	0.014	0.0	10.5
	B20s0	0.0	0	10^{-3}	−1.8	9.37
	B20s4	0.4	260	10^{-3}	−1.8	11.1
	C20s0	0.0	0	10^{-5}	−3.8	9.28
	C20s4	0.4	305	10^{-5}	−3.8	10.8
25	A25s0	0.0	0	0.014	0.0	7.19
	A25s4	0.4	214	0.014	0.0	8.43
	B25s0	0.0	0	10^{-3}	−1.8	7.62
	B25s4	0.4	285	10^{-3}	−1.8	8.85
	C25s0	0.0	0	10^{-5}	−3.8	7.53
	C25s4	0.4	333	10^{-5}	−3.8	8.68
	C25s4b[a]	0.4	333	10^{-5}	−3.8	8.68
	C25s5	0.5	428	10^{-5}	−3.8	8.85
	C25s5b[a]	0.5	428	10^{-5}	−3.8	8.85
	D25s0	0.0	0	10^{-7}	−5.8	7.18
	D25s4	0.4	383	10^{-7}	−5.8	8.26
	D25s4b[a]	0.4	383	10^{-7}	−5.8	8.26
	D25s6	0.6	588	10^{-7}	−5.8	8.70
	D25s6b[a]	0.6	588	10^{-7}	−5.8	8.70
40	A40s4	0.4	186	0.014	0.0	5.75
	B40s4	0.4	334	10^{-3}	−1.8	5.99
	C40s4	0.4	409	10^{-5}	−3.8	5.89

Note. [a]Models calculated with a lower ^{17}O(α, γ), see the text for details.

sequence $\langle\upsilon\rangle_{\rm MS} = 200$–$220\,{\rm km\,s^{-1}}$. This is slightly lower than the peak of the velocity distribution, at $\upsilon_{\rm MW,\,peak} = 225\,{\rm km\,s^{-1}}$, found for O- and B-type stars in the Milky Way (Dufton et al. 2006; Hunter et al. 2009). Due to their low metal content, low-Z massive stars are more compact and have a higher surface velocity than their equivalents found in the Milky Way. With $\upsilon_{\rm ini}/\upsilon_{\rm crit} =$ constant, $\langle\upsilon\rangle_{\rm MS}$ increases with decreasing Z up to about $400\,{\rm km\,s^{-1}}$. This view of faster rotating massive stars at low Z is supported by observations of an increasing Be/B-type star ratio with decreasing metallicity (Maeder, Grebel & Mermilliod 1999; Martayan et al. 2007), by faster rotating massive stars in the SMC compared to the Milky Way (Hunter et al. 2008) and hydrodynamic models of the first generation of stars (Stacy, Bromm & Loeb 2011). Thus, $\upsilon_{\rm ini}/\upsilon_{\rm crit}$ being constant is a conservative choice and might turn out to be too slow to reproduce the peak velocity of the velocity distribution at low Z, which is unknown. We assess the possible impact of faster rotation at low Z by models C25s5 and D25s6 with $\upsilon_{\rm ini}/\upsilon_{\rm crit} = 0.5$ and 0.6, respectively.

More details about the models, a script to fit reaction rates in the REACLIB format and a script to generate initial abundance sets for a given metallicity are available upon request and are described in Frischknecht (2012).

2.2 Yield calculations

In this work, a complete list of pre-supernova (pre-SN) yields is determined. The total pre-SN yields include a wind and a supernova-progenitor contribution. The pre-SN yield of a nucleus i is the net amount produced of it in $\rm M_\odot$ and can easily be calculated by

$$m_i = \int_{M_{\rm rem}}^{M^*} (X_i(M) - X_{i,0}){\rm d}M + \int_0^\tau \dot{M}(t)(X_{i,{\rm s}}(t) - X_{i,0}){\rm d}t, \quad (1)$$

where M^* is the stellar mass before the explosion, $X_i(M)$ the mass fraction of nucleus i at Lagrangian mass coordinate M, $X_{i,0}$ the initial mass fraction, $X_{i,{\rm s}}$ the surface mass fraction and $\dot{M}$ the mass-loss rate. The first term on the left-hand side describes the mass produced or destroyed in the supernova-progenitor and the second term describes what is ejected by the wind. The remnant mass $M_{\rm rem}$ was derived from the relation of $M_{\rm rem}$ to $M_{\rm CO}$, which was originally established in Maeder (1992). $M_{\rm CO}$ is the carbon–oxygen core mass determined as the part of the star for which the ^{4}He mass fraction is below 10^{-2}. Both, $M_{\rm rem}$ and $M_{\rm CO}$, are listed in Table 2 in units of $\rm M_\odot$, as well as the final mass, $M_{\rm fin}$, the mass coordinate for which $X(^4{\rm He}) > 0.75$, M_α, the maximal extension of the convective He-core $M_{\rm He}^{\rm max}$ and the maximal mass of convective C-burning shell $M_{\rm C}^{\rm max}$. The latter is given because this is the maximal mass coordinate at which the s-process produced in the C-shell can be mixed outwards.

The time-scales of C-burning and later evolutionary stages are much shorter than those of H- and He-burning stages. Our models were calculated at least up to the onset of O-burning; hence, the wind contribution in equation (1) is fully determined by our models. The pre-SN term in equation (1) was calculated from the final profile during O-burning. Changes in the chemical profile during the final phase appear only in the innermost part of the star. We compared our models with Hirschi, Meynet & Maeder (2004) and even though our models do not use exactly the same mixing and wind prescription, the lower boundary and the extension of the C-shell as well as the size of convective core during O-burning are similar. We therefore know that our models would evolve in a similar way as the one of Hirschi et al. (2004), up to the onset of core collapse. In this case, we expect only a weak modification of the yields for the $15\,\rm M_\odot$ star. Thus, we are confident that running the models only up to O-burning is sufficient for a good approximation of the pre-explosive yields.

The yields from the SN progenitor are modified by explosive nucleosynthesis activated by SN shock (e.g. Thielemann, Nomoto & Hashimoto 1996). The total yields of s-process nuclei are not strongly modified by the explosion (e.g. Tur, Heger & Austin 2009). Therefore, the yields calculated here can be taken as a good estimate and are well suited to investigate the galactic chemical enrichment in s-process nuclei and light nuclei by massive rotating stars.

We calculated the yields separately for core He-, shell He- and shell C-burning to distinguish between these three contributions to the s-process production. For this purpose, we calculated the yields both at the end of core He-burning (He-core contribution) and at the pre-SN stage considering only the material above the final mass cut, $M_{\rm r} > M_{\rm rem}$, as illustrated in Fig. 1. The separate contributions from shell He- and shell C-burning are obtained by splitting the pre-SN yields into two parts at mass $M_{\rm C-He}$ (red horizontal line in Fig. 1). ^{20}Ne is a C-burning product and its abundance drop at the outer

Table 2. Final total mass and different core masses of the models

Model	$M_{\rm fin}$	M_α	$M_{\rm He}^{\rm max}$	$M_{\rm C}^{\rm max}$	$M_{\rm CO}$	$M_{\rm rem}^a$
A15s0	13.01	4.27	2.24	2.19	2.35	1.49
A15s4	10.43	5.81	3.39	2.75	3.33	1.74
B15s0	14.80	4.74	2.60	2.33	2.62	1.56
B15s4	13.84	6.03	3.52	2.54	3.44	1.77
C15s0	14.99	4.54	2.41	2.02	2.49	1.52
C15s4	14.84	5.70	3.41	2.06	3.34	1.74
A20s0	9.02	6.17	3.84	3.23	3.76	1.85
A20s4	7.92	7.88	5.36	3.41	5.13	2.20
B20s0	19.85	6.65	4.15	3.75	4.11	1.94
B20s4	10.91	8.16	5.41	4.35	5.22	2.22
C20s0	20.00	6.26	3.93	3.54	3.88	1.88
C20s4	17.01	8.10	5.36	3.82	5.18	2.21
A25s0	10.86	8.23	5.74	4.87	5.53	2.30
A25s4	10.04	9.99	7.40	5.97	6.97	2.66
B25s0	24.73	8.63	5.92	4.97	5.79	2.36
B25s4	14.32	10.96	7.93	6.62	7.56	2.81
C25s0	25.00	8.03	5.61	4.47	5.57	2.31
C25s4	24.34	10.69	7.63	5.07	7.33	2.75
C25s4b[b]	24.34	10.69	7.65	6.33	7.25	2.73
C25s5	24.72	10.49	7.38	5.59	7.08	2.69
C25s5b[b]	24.38	10.49	7.37	5.10	7.12	2.70
D25s0	25.00	7.39	5.72	4.09	5.56	2.31
D25s4	25.00	8.77	5.78	4.97	5.61	2.32
D25s4b[b]	25.00	8.77	5.80	4.49	5.56	2.31
D25s6	24.81	9.72	6.53	3.92	6.19	2.46
D25s6b[b]	24.81	9.71	6.52	4.27	6.29	2.49
A40s4	19.01	19.01[c]	15.23	14.10	15.04	4.65
B40s4	25.15	19.30	15.40	13.90	14.76	4.57
C40s4	38.49	19.18	14.70	6.51	14.08	4.36

Notes. [a]$M_{\rm rem}$ is estimated following the relation established in Maeder (1992).
[b]Models calculated with a lower $^{17}{\rm O}(\alpha,\gamma)$, see Section 2.1 for details.
[c]This star ends its life as WR star and as a consequence $M_\alpha = M_{\rm fin}$.

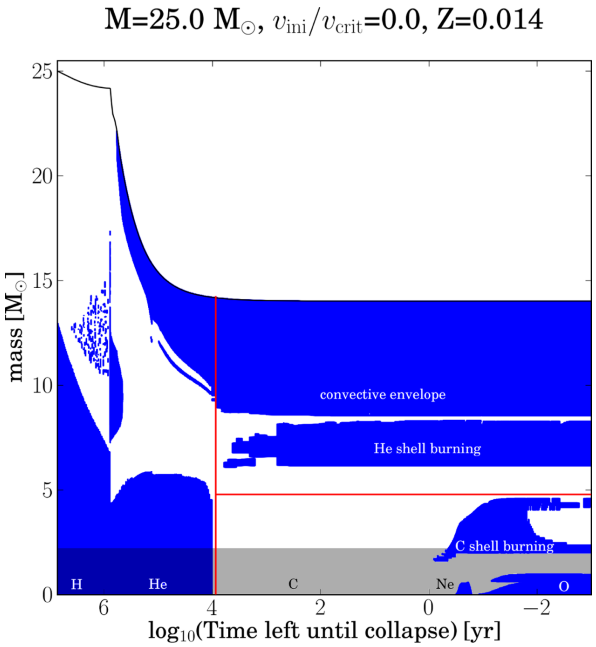

Figure 1. Kippenhahn diagram of 25 $M_\odot$ star with $Z = Z_\odot$ and no rotation (A25s0), to illustrate the M_{C-He} (red horizontal line). The shaded areas show the mass ending up inside M_{rem}. The red vertical line marks the point in the stellar life where the core He *s*-process yields are calculated.

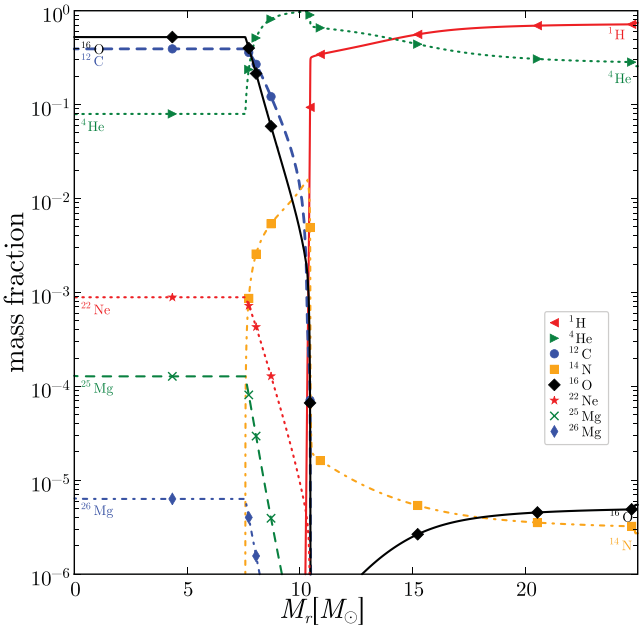

Figure 2. Abundance profiles of the main light isotopes during central He-burning (X_c(He) ≈ 0.08) for the 25 $M_\odot$ model with rotation and $Z = 10^{-5}$ (C25S4). The convective He-burning core extends from the centre to about $M_r = 7.5\,M_\odot$ (flat abundance profiles). The bottom of hydrogen shell burning is just above 10 $M_\odot$ (sudden drop of hydrogen abundance). Rotation-induced mixing brings freshly produced ^{12}C and ^{16}O from the core into contact with the hydrogen burning shell, where a peak a primary nitrogen (^{14}N) develops. Further mixing (both convective and rotation-induced) brings the primary nitrogen down into the He-burning core where it is transformed into ^{22}Ne, leading to primary production of both ^{14}N and ^{22}Ne.

boundary of the C-burning shell was chosen to determine M_C^{max}, and finally we set $M_{C-He} = M_C^{max} + 0.01$.

Besides the yields, the production factors, *f*, will be used in the subsequent discussion. The production factor of an isotope *i* is defined as

$$f_i = \frac{m_{i,\mathrm{eject}}}{m_{i,\mathrm{ini}}} = \frac{m_i + m_{i,\mathrm{ini}}}{m_{i,\mathrm{ini}}},$$

with m_i the total yield from equation (1), $m_{i,\,\mathrm{eject}}$ the ejected mass and $m_{i,\,\mathrm{ini}}$ the initial mass of nucleus *i* in the star. The production factor quantifies if a star is a strong producer of an element or not.

The yields are available on http://www.astro.keele.ac.uk/shyne/datasets.

3 ROTATION-INDUCED MIXING AND PRODUCTION OF PRIMARY ^{22}NE AND ^{14}N

Meynet & Maeder (2002a,b) and Hirschi (2007) find that rotating stars produce important amounts of primary ^{14}N and ^{22}Ne via rotation-induced mixing. The production of these nuclei originates from the transport of matter between the He-burning core and the H-burning shell. If the He-burning products ^{12}C and ^{16}O reach the proton-rich layers, they are burnt immediately into ^{14}N via the CNO cycle. An ^{14}N-rich zone is produced in this way at the lower edge of the H-burning shell as shown in Fig. 2. Some of this nitrogen is transported back into the He-burning core, where it is further transformed into ^{22}Ne via two α-captures. In this section, we attempt to answer the following questions: Under which conditions is the transport of chemical elements efficient? How much ^{22}Ne and ^{14}N is produced in massive stars?

3.1 Helium core burning

The transport of chemical elements is illustrated for the 25 $M_\odot$ model with rotation at $Z = 10^{-5}$ in Fig. 2, which shows the abundance profiles in this model during core He-burning. The rotation-induced mixing, which leads to the production of primary ^{14}N and ^{22}Ne, occurs in the region above the convective He-core ($M_r \approx 7.5$–$10.5\,M_\odot$). The core itself is identifiable by the flat abundance profile between $M_r = 0$ and $7.5\,M_\odot$. Differential rotation develops between the convective He-core and H-shell mainly because of the core contraction and envelope expansion at the end of the main sequence. The differential rotation induces secular shear mixing in this radiative zone, in which no mixing would take place in non-rotating models. Shear mixing, a diffusive process, brings primary ^{12}C and ^{16}O (blue dashed and black continuous lines) into contact with the H-burning layer and creates an ^{14}N-pocket ($M_r \approx 7.5$–$10.5\,M_\odot$) via the CNO cycle as explained above. In our models, the transport of ^{14}N back to the centre is mainly due to the growth of the convective core, incorporating parts of the ^{14}N-pocket. Indeed, the diffusive transport is not fast enough to produce an ^{22}Ne mass fraction, $X(^{22}\mathrm{Ne})$, of 10^{-3}–10^{-2} in the core, necessary to boost the *s*-process significantly.

Secular shear is the main mechanism for the transport between He-core and H-envelope. The diffusion coefficient, D_{shear}, used in the models presented here is the coefficient of Talon & Zahn (1997) and is given by

$$D_{\mathrm{shear}} = \frac{(K + D_{\mathrm{h}})}{\left[\frac{\varphi}{\delta}\nabla_\mu(1 + \frac{K}{D_{\mathrm{h}}}) + (\nabla_{\mathrm{ad}} - \nabla_{\mathrm{rad}})\right]} \times \frac{\alpha H_{\mathrm{p}}}{g\delta}\left(\frac{9\pi}{32}\Omega\frac{\mathrm{d}\ln\Omega}{\mathrm{d}\ln r}\right)^2.$$

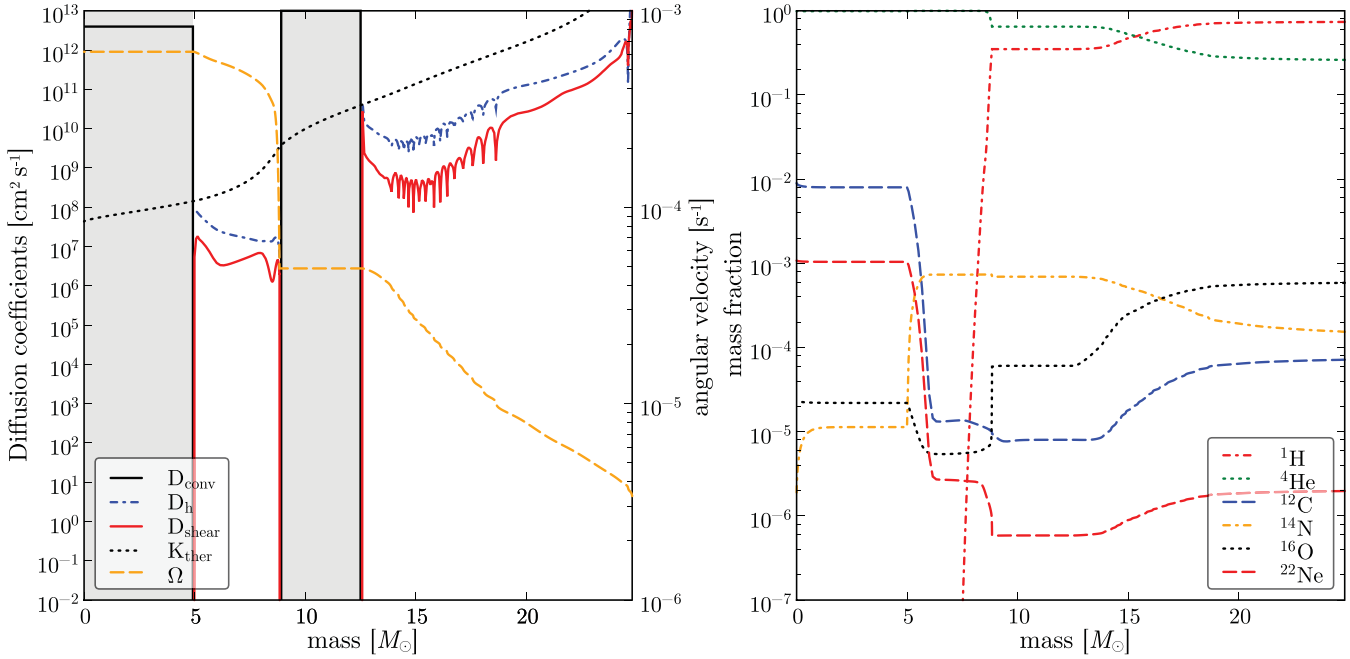

Figure 3. Diffusion coefficient profiles on the left-hand side and abundance profiles on the right-hand side during central He-burning, when a convective H-shell is present, inside the 25 $M_\odot$ star with rotation at $Z = 10^{-3}$ (B25S4). The shear diffusion coefficient (red continuous line) is responsible for the mixing between He-core and H-shell. The convective regions are represented by the grey shaded areas.

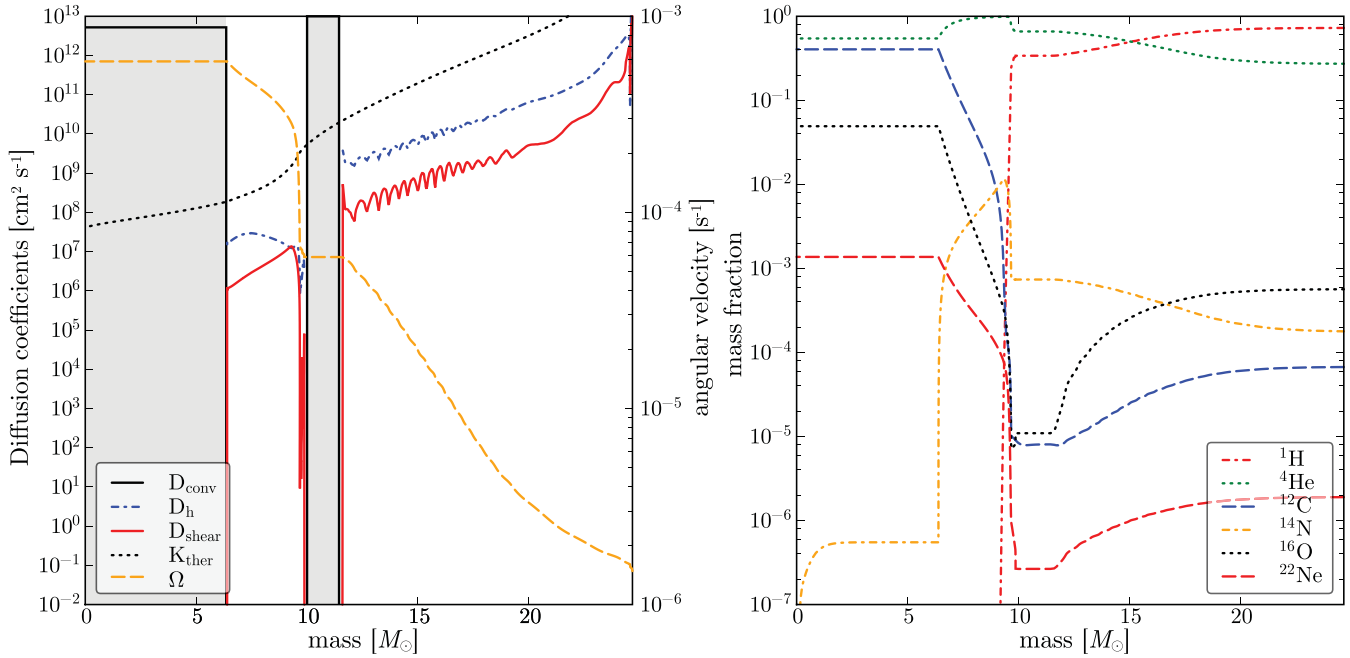

Figure 4. Diffusion coefficient profiles on the left-hand side and abundance profiles on the right-hand side during central He-burning, when a retracting convective H-shell is present, inside the 25 $M_\odot$ star with rotation at $Z = 10^{-3}$ (B25S4). The shear diffusion coefficient (red continuous line) describes the mixing between He-core and H-shell. The convective regions are represented by the grey shaded areas.

Naturally, high Ω-gradient and Ω favour shear. The presence of a mean molecular weight gradient, ∇_μ, on the other hand, has a stabilizing effect on shear mixing. Such a ∇_μ is present between H-burning shell and He-rich core and is most prominent at the lower edge of the H-burning zone. Using the formula of Talon & Zahn (1997), D_{shear} is lowered most efficiently where the thermal diffusivity, K, is larger than the horizontal turbulence, D_h ($K > D_h$). In our models, just above the convective He-core, where K/D_h has typical values between 10 and 100, and where ∇_μ is highest, the term including ∇_μ reaches values up to 10^3, which shows the strong inhibiting effect of μ-gradients on mixing. This can also be seen on the left-hand side in Figs 3, 4 and 5 at $M_r \approx 5$–$10\,M_\odot$, where K is the black dotted line and D_h is the blue dash–dotted line. The K/D_h ratio does not change significantly in the relevant regions in

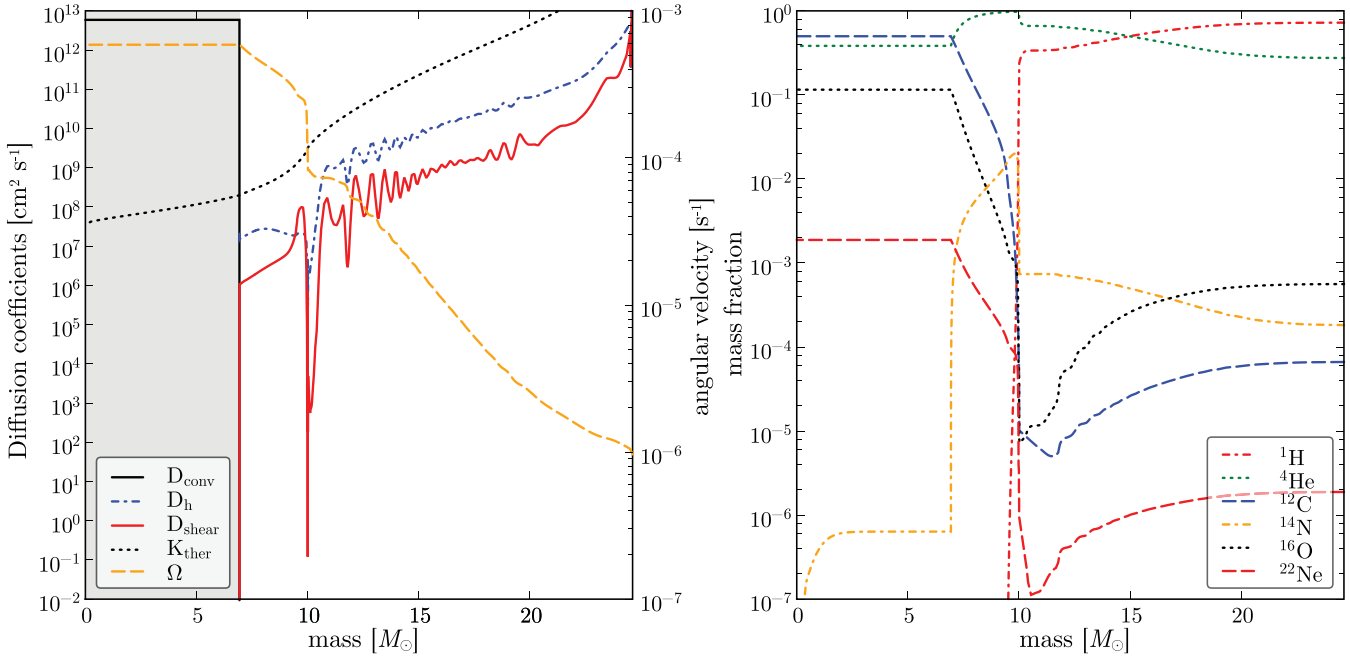

Figure 5. Diffusion coefficient profiles on the left-hand side and abundance profiles on the right-hand side during central He-burning, when no convective H-shell is present, inside the 25 $M_\odot$ star with rotation at $Z = 10^{-3}$ (B25S4). The shear diffusion coefficient (red continuous line) describes the mixing between He-core and H-shell. The convective core is represented by the grey shaded areas.

the course of central He-burning. Regions of strong μ-gradients can be identified by steep slopes in the abundance of hydrogen and carbon on the right-hand side of these figures as discussed below. There are other formulae for shear mixing, which might lead to different mixing efficiencies. For example, in the formula of Maeder (1997) for D_{shear}, the prefactor $(1 + \frac{K}{D_h})$ is not present and the inhibiting effect of the μ-gradient is weaker, which means that the shear mixing would be stronger had we used that formula. If the Tayler–Spruit dynamo due to magnetic fields were considered as in for example Heger, Woosley & Spruit (2005), mixing would also be stronger and often leads to a quasi-homogeneous chemical evolution of rotating low-Z stars (Yoon, Langer & Norman 2006). The mixing considered in this study is thus conservative and mixing could be stronger.

In the grid of models including the effects of rotation that we have calculated, there are three different configurations of the stellar structure that may occur during central He-burning. These cases are illustrated with the help of three evolutionary snapshots of a rotating 25 $M_\odot$ $Z = 10^{-3}$ star during central He-burning.

(i) Case (a): in the first configuration, shown in Fig. 3, the convective H-burning shell ($M_r \approx 9$–$13\,M_\odot$) rotates considerably slower than the regions below (the angular velocity Ω profile is plotted as an orange dashed line on the left-hand side). The steep gradient of Ω at the lower boundary of the convective shell compensates for the inhibiting effect of ∇_μ, which is strongest just below the convective shell where the gradient of hydrogen abundance is very steep. In this configuration, D_{shear} has values between 10^4 and 10^7 cm^2 s^{-1} throughout the radiative region between the convective He-core and the H-shell zones, facilitating a strong production of primary nitrogen.

(ii) Case (b): this configuration shown in Fig. 4 is very similar to case (a), i.e. there is a convective H-burning shell but with the important difference that the convective H-shell is moving away from its lowest mass coordinate. The upward migration of the lower boundary leaves a shallow Ω-gradient behind, at $M_r \approx 9.5\,M_\odot$ on the left-hand side in Fig. 4. In this case, the steep Ω-gradient and the μ-gradient do not coincide, and a region with low values of D_{shear} develops, i.e. D_{shear} between 10 and 10^4 cm^2 s^{-1}. The mixing across the bottom of the convective shell is thus less efficient and abundance gradients are steeper below the convective shell (just below 10 $M_\odot$ in the right-hand panel of Fig. 4)

(iii) Case (c), shown in Fig. 5, is the case with no convective zone in the H-rich layers and only a moderate Ω-gradient across the H-burning shell. At the mass coordinate, where abundance gradients are steepest (at 10 $M_\odot$ in the right-hand panel of Fig. 5), the shear diffusion coefficient is weakest, with D_{shear} between 1 and 10^3 cm^2 s^{-1}. During helium burning, case (c) may follow case (b). In this situation, the Ω-gradient is even lower at the bottom of the H-burning shell and D_{shear} has the lowest values. If there is no convective H-burning shell, then case (c) is the only case the model goes through.

The rotating solar metallicity 15, 20 and 25 $M_\odot$ models, as well as the 15 $M_\odot$ with sub-solar Z, do not develop a convective zone at the inner edge of the hydrogen-rich layers during central He-burning. Thus, mixing in these models corresponds to case (c). The rotating sub-solar Z models with 20, 25 and 40 $M_\odot$, as well as the 40 $M_\odot$ $Z = Z_\odot$ model, develop before the start of central He-burning a convective H-shell where the H-shell burning occurs. It shrinks and retreats when the convective He-core grows. These models follow therefore the sequence: (a)-(b)-(c), but with a basic difference between the models at $Z = 10^{-5}$ and those at higher metallicity. While the latter develop case (b) with a very low D_{shear} as soon as the convective shell starts to shrink, the former show strong angular momentum transport at the steep Ω-gradient, which is fast enough to follow the retreating convective zone and therefore develops rather a hybrid case between (a) and (b) when the

Table 3. ^{14}N and ^{22}Ne production and destruction. See the text for explanations.

Model	$\Delta X(^{22}\mathrm{Ne})^a$	$X_\mathrm{r}(^{22}\mathrm{Ne})^a$	$X_\mathrm{shell}(^{22}\mathrm{Ne})^a$	$m(^{22}\mathrm{Ne})^a$ ($\mathrm{M}_\odot$)	$m(^{14}\mathrm{N})^a$ ($\mathrm{M}_\odot$)
A15s0	3.06(−3)	9.70(−3)	9.23(−3)	9.11(−3)	3.19(−2)
A15s4	5.59(−3)	7.42(−3)	1.38(−2)	2.78(−2)	2.63(−2)
B15s0	3.54(−4)	8.02(−4)	9.24(−4)	1.28(−3)	2.91(−3)
B15s4	9.37(−4)	1.02(−3)	7.34(−3)	1.49(−2)	7.17(−3)
C15s0	3.75(−6)	7.70(−6)	1.02(−5)	6.42(−5)	4.77(−5)
C15s4	4.84(−4)	3.92(−4)	7.55(−3)	1.39(−2)	5.25(−3)
A20s0	5.34(−3)	7.43(−3)	1.14(−2)	2.50(−2)	3.76(−2)
A20s4	7.23(−3)	5.03(−3)	1.99(−2)	4.99(−2)	3.72(−2)
B20s0	6.16(−4)	5.46(−4)	1.15(−3)	2.68(−3)	4.06(−3)
B20s4	3.49(−3)	1.14(−3)	3.20(−2)	7.59(−2)	9.39(−3)
C20s0	5.66(−6)	5.74(−6)	1.32(−5)	1.21(−4)	5.80(−5)
C20s4	1.52(−3)	4.62(−4)	1.67(−2)	4.09(−2)	4.04(−3)
A25s0	7.68(−3)	5.10(−3)	1.27(−2)	3.39(−2)	4.76(−2)
A25s4	9.69(−3)	3.28(−3)	1.56(−2)	4.06(−2)	4.95(−2)
B25s0	7.52(−4)	4.16(−4)	1.15(−3)	3.36(−3)	5.90(−3)
B25s4	4.08(−3)	6.22(−4)	1.99(−2)	6.72(−2)	8.47(−3)
C25s0	7.21(−6)	4.14(−6)	1.13(−5)	2.38(−4)	9.38(−5)
C25s4	1.23(−3)	1.69(−4)	1.15(−2)	3.61(−2)	1.85(−3)
C25s4b[b]	1.27(−3)	1.82(−4)	1.17(−2)	3.49(−2)	9.33(−4)
C25s5	3.83(−3)	4.94(−4)	1.59(−2)	4.80(−2)	2.07(−3)
C25s5b[b]	3.75(−3)	4.85(−4)	1.61(−2)	4.81(−2)	1.99(−3)
D25s0	8.28(−7)	4.67(−7)	3.09(−7)	1.63(−4)	1.80(−5)
D25s4	1.05(−4)	3.81(−5)	1.46(−2)	3.81(−2)	1.10(−2)
D25s4b[b]	1.06(−4)	3.96(−5)	1.45(−2)	3.71(−2)	1.11(−2)
D25s6	4.57(−3)	2.68(−4)	1.95(−2)	5.52(−2)	3.43(−3)
D25s6b[b]	4.44(−3)	3.11(−4)	2.00(−2)	5.56(−2)	3.48(−3)
A40s4	1.23(−2)	5.29(−4)	1.21(−2)	3.34(−2)	2.23(−2)
B40s4	3.31(−3)	1.06(−4)	2.08(−2)	7.99(−2)	1.84(−2)
C40s4	2.70(−3)	1.93(−5)	8.75(−3)	3.21(−2)	2.07(−3)

Notes. [a]Values in parentheses are the exponents ($x(y) = x \times 10^y$).
[b]This model was calculated with the same initial parameters as the model, on the line above, but with the ^{17}O(α, γ) reaction rate of CF88 divided by 10.

convective shell shrinks. The mixing is thus strongest in $Z = 10^{-5}$ models, followed by sub-solar Z models with 20, 25 and 40 $\mathrm{M}_\odot$ and the 40 $\mathrm{M}_\odot$ $Z = \mathrm{Z}_\odot$ model, and finally followed by the $\mathrm{Z}_\odot$ 15, 20 and 25 $\mathrm{M}_\odot$ models and the sub-solar 15 $\mathrm{M}_\odot$ models. To ensure that the mixing does not depend strongly on our choice of resolution parameters, a 25 $\mathrm{M}_\odot$ $Z = 10^{-3}$ rotating model was performed with a much higher resolution, i.e. doubled resolution in the He-core[1] and five times the resolution in the radiative layers between the convective core and H-burning shell.[2] The model with higher resolution had a smoother growth of the convective core but it did not affect the ^{14}N and ^{22}Ne production strongly. For example, the mass fractions $\Delta X(^{22}\mathrm{Ne})$ of burned ^{22}Ne during central He-burning decreased only by 2.5 per cent in the high-resolution model compared to the standard resolution. The mass fraction $X_\mathrm{shell}(^{22}\mathrm{Ne})$ of ^{22}Ne in the He-shell at the pre-SN stage differed by 22 per cent (lower): $X(^{22}\mathrm{Ne}) = 0.0246$ and 0.0314, for the high- and the default-resolution model, respectively. The slight decrease of transport efficiency when using a higher resolution therefore does not change the *s*-process and only moderately lower the yields of ^{14}N and ^{22}Ne. These differences due to resolution are very small compared to the differences between non-rotating and rotating models (see Table 3).

Since ^{22}Ne is produced and destroyed at the same time in rotating stars, we derived the amount of ^{22}Ne burned during central He-burning from the sum of the ^{25}Mg and ^{26}Mg produced during this stage.

In Table 3, the mass fractions $\Delta X(^{22}\mathrm{Ne})$ of burned ^{22}Ne during central He-burning, $X_\mathrm{r}(^{22}\mathrm{Ne})$ of remaining ^{22}Ne after He-burning, $X_\mathrm{shell}(^{22}\mathrm{Ne})$ of ^{22}Ne in the He-shell at the pre-SN stage, and the yields of ^{22}Ne and ^{14}N are tabulated for all models. $\Delta X(^{22}\mathrm{Ne})$ is the ^{22}Ne destroyed mainly by the (n,γ) and α-capture channels, where the (α,n) channel is the *s*-process neutron source in He-burning. $X_\mathrm{r}(^{22}\mathrm{Ne})$ is the ^{22}Ne left in the He-core ashes, and it will be destroyed mostly by the (p,γ) and (α,n) channels during C-burning (e.g. Pignatari et al. 2010).

We can see from Table 3 ($\Delta X(^{22}\mathrm{Ne}$, burned)) that rotating models at all metallicities produce and burn significant amounts of ^{22}Ne, confirming the results of previous studies (Meynet et al. 2006; Hirschi 2007). At solar metallicity, ^{22}Ne is predominantly secondary. At low metallicities, in the models including rotation, mixing is strong enough to produce a pocket of primary ^{14}N above the convective core, which is then converted to primary ^{22}Ne. The amount of primary ^{22}Ne in the convective He-core at the end of He-burning, when *s*-process is activated, is between 0.1 and 1 per cent

[1] The critical value of the luminosity gradient ΔL_crit, used to split a mass shell when $\Delta L > \Delta L_\mathrm{crit}$, was reduced by a factor of 2.
[2] The critical values of the mass fraction gradients of carbon and helium, $\Delta X_\mathrm{crit}(^{12}\mathrm{C})$ and $\Delta X_\mathrm{crit}(^{4}\mathrm{He})$, used to split a mass shell when $\Delta X(^{12}\mathrm{C}) > \Delta X_\mathrm{crit}(^{12}\mathrm{C})$ or $\Delta X(^{4}\mathrm{He}) > \Delta X_\mathrm{crit}(^{4}\mathrm{He})$, were reduced by a factor of 5.

in mass fractions. Considering a constant value of $\upsilon_{\rm ini}/\upsilon_{\rm crit} = 0.4$ at all metallicities, the primary ^{22}Ne in the He-core decreases slightly with decreasing metallicity. There is, however, theoretical and observational support to consider a slight increase of $\upsilon_{\rm ini}/\upsilon_{\rm crit}$ with decreasing metallicity as discussed in the previous section. We thus also computed models with 25 $M_\odot$ and $\upsilon_{\rm ini}/\upsilon_{\rm crit} = 0.4$ at $Z = Z_\odot$ and 10^{-3}, $\upsilon_{\rm ini}/\upsilon_{\rm crit} = 0.5$ at $Z = 10^{-5}$ and $\upsilon_{\rm ini}/\upsilon_{\rm crit} = 0.6$ at $Z = 10^{-7}$, which correspond to a slight increase of $\upsilon_{\rm ini}/\upsilon_{\rm crit}$ with decreasing metallicity. Considering a slightly increasing initial rotation rate with decreasing metallicity, rotating models produce and burn a constant quantity of ^{22}Ne, around 0.5 per cent in mass fraction, almost independent of the initial metallicity. These results show that significant amounts of ^{22}Ne are expected to be produced in massive rotating stars over the entire range of masses and all metallicities.

3.2 Helium shell burning

The convective He-shell, which follows on the ^{14}N-rich zone, transforms most of this ^{14}N into ^{22}Ne. While the ^{22}Ne in the He-shell of non-rotating model is purely secondary, in rotating models it is primary at the pre-SN stage and almost independent of metallicity. The ^{22}Ne is only partially destroyed during the He-shell burning and there is a mass fraction of $X(^{22}\mathrm{Ne})$ between 0.7 and 3.2 per cent in the He layers at the pre-SN stage. This is relevant for explosive neutron capture nucleosynthesis in He-shell layers. This site was investigated by Blake & Schramm (1976), Truran, Cowan & Cameron (1978) and Thielemann, Arnould & Hillebrandt (1979) as a possible *r*-process scenario, but later on found to be unlikely (Blake et al. 1981). Instead, the explosive shell He-burning in core-collapse supernovae is hosting the *n*-process (e.g. Blake & Schramm 1976), with typical abundance signatures identified in presolar silicon-carbide grains of type X (e.g. Meyer, Clayton & The 2000; Zinner 2014). It will be worthwhile to explore in the future the impact of these large amounts of primary ^{22}Ne produced in rotating models at all *Z*, for explosive neutron capture nucleosynthesis.

3.3 Carbon shell burning

Carbon shell burning is the second efficient *s*-process production site inside massive stars at solar metallicity (e.g. Raiteri et al. 1991b; Rauscher et al. 2002; The, El Eid & Meyer 2007; Pignatari et al. 2010). One could think of rotation-induced mixing appearing in the same way as in He-burning, mixing down some of the primary ^{22}Ne into the C-shell and boosting the *s*-process. However, the time-scale of the secular shear mixing, which is still present between convective He- and C-shells, is of the same order as during central He-burning. On the other hand, the burning time-scales of Ne, O and Si burning are at least five to six orders of magnitude smaller than the one of He-burning. This implies that the ^{22}Ne available to make neutrons via the ^{22}Ne(α,n) reaction in the convective C-burning shell is what is left in the ashes of the previous convective He-core, like in non-rotating models.

Rotation, however, affects the CO-core sizes and the ^{12}C/^{16}O ratio after He-burning (e.g. Hirschi et al. 2004). This will indirectly affect all subsequent burning phases and their heavy element production.

4 STANDARD WEAK *s*-PROCESS IN STARS

In Table 4, several characteristic quantities for *s*-process in He-burning are presented. Note that some of these quantities are averaged quantities over the convective core and integrated over the helium-burning phase, encompassing in one number complex processes varying both in space and in time. These quantities are useful in the sense that they allow through a unique number to see the importance of different phases, and also to compare the outputs of different models.

In a one-zone model, a useful quantity is the neutron exposure defined as

$$\tau = \int_{t_{\rm ini-He}}^{t_{\rm end-He}} \upsilon_{\rm T} n_{\rm n} {\rm d}t, \tag{2}$$

where $t_{\rm ini-He}$ and $t_{\rm end-He}$ are the age of the star at the beginning and the end of the core He-burning phase, respectively, $n_{\rm n}$ the neutron density and $\upsilon_{\rm T}$ the thermal velocity, $\upsilon_{\rm T} = \sqrt{2kT/m_{\rm n}}$ with $kT =$ 30 keV. The value of 30 keV is typical of the conditions at the end of the core He-burning phase.

In multiple-zone simulations, as in stellar models, the neutron number density, $n_{\rm n}$, varies with time and the mass coordinate in the star. For the investigation of *s*-process in convective zones, one can define a mean or effective neutron exposure

$$\langle\tau\rangle = \int \langle n_{\rm n}(t)\rangle \upsilon_{\rm T} {\rm d}t. \tag{3}$$

In equation (3), $\langle n_{\rm n}(t)\rangle$ is an average over the convective core. Such a global quantity has to be interpreted with caution since in reality the neutrons are captured locally during core He-burning, near the centre of the star and later the *s*-process products are mixed outwards.

Another characteristic *s*-process quantity is the average number of neutron captures per iron ($Z = 26$) seed (e.g. Käppeler et al. 1990)

$$n_{\rm c} = \frac{\sum_{A=56}^{209} (A-56)\,(Y(A) - Y_0(A))}{\sum_{Z=26} Y_0(A)}, \tag{4}$$

where $Y(A)$ and $Y_0(A)$ are the final and the initial number abundance, respectively, of a nucleus with nuclear mass number *A*. Additionally, the core-averaged ($\bar{n}_{\rm n,max}$) and central ($n_{\rm n,c,max}$) peak neutron density, the amount of ^{22}Ne burnt during He-burning ($\Delta X(^{22}\mathrm{Ne})$) and the amount of ^{22}Ne left in the centre at core He exhaustion ($X_{\rm r}(^{22}\mathrm{Ne})$) are tabulated.

4.1 He-core burning

Let us begin by discussing the solar metallicity models. Due to ^{14}N transformation at the beginning of the core He-burning phase, all models had initially in the He-core[3] about $X(^{22}\mathrm{Ne}) = 1.3 \times 10^{-2}$. The abundance of ^{22}Ne will not change during a large fraction of the core He-burning phase. Only close to the end of central He-burning, part of the ^{22}Ne will be transformed into ^{25}Mg and ^{26}Mg. When the temperatures for an efficient activation of ^{22}Ne(α, n)^{25}Mg are reached, some ^{22}Ne has already been destroyed by the (α, γ)^{26}Mg reaction. More quantitatively, when $T_8 \approx 2.8$ is reached (temperature, at which the (α, n) channel starts to dominate), only $X(^{22}\mathrm{Ne}) = 10^{-2}$, 6.8×10^{-3}, 5.7×10^{-3} and 5.0×10^{-3} is left in models A15s0, A25s0, A25s4 and A40s4, respectively.

Important well-known aspects of the *s*-process during core He-burning are the following.

[3] i.e. before ^{22}Ne is destroyed by the two reactions ^{22}Ne(α, n) and ^{22}Ne(α, γ).

Table 4. *s*-process parameters at central He exhaustion.

Model[a]	τ_c[b] (mb^{-1})	$\langle\tau\rangle$[c] ($10^{-1}\,mb^{-1}$)	n_c[d]	$\bar{n}^e_{n,max}$ (cm^{-3})	$n_{n,c,max}$[f,g] (cm^{-3})	$\Delta X(^{22}Ne)$[g]	$X_r(^{22}Ne)$[g]
A15s0	1.52	0.581	0.77	3.04(5)	6.58(6)	3.06(−3)	9.70(−3)
A15s4	2.93	1.02	1.60	4.65(5)	1.17(7)	5.59(−3)	7.42(−3)
B15s0	0.883	0.427	0.53	2.32(5)	4.32(6)	3.54(−4)	8.02(−4)
B15s4	3.06	1.51	2.55	5.18(5)	1.07(7)	9.37(−4)	1.02(−3)
C15s0	0.0157	0.0561	0.04	2.85(3)	5.59(4)	3.75(−6)	7.70(−6)
C15s4	2.21	1.07	2.18	3.38(5)	7.33(6)	4.84(−4)	3.92(−4)
A20s0	2.97	0.971	1.52	5.17(5)	1.22(7)	5.34(−3)	7.43(−3)
A20s4	4.66	1.43	2.57	5.89(5)	1.54(7)	7.23(−3)	5.03(−3)
B20s0	1.88	0.761	1.13	4.11(5)	9.10(6)	6.16(−4)	5.46(−4)
B20s4	9.73	4.07	9.85	8.73(5)	2.22(7)	3.49(−3)	1.14(−3)
C20s0	0.0286	0.0401	0.05	6.00(3)	1.31(5)	5.66(−6)	5.74(−6)
C20s4	6.55	2.80	5.87	6.84(5)	1.69(7)	1.52(−3)	4.62(−4)
A25s0	4.42	1.33	2.42	5.85(5)	1.56(7)	7.68(−3)	5.10(−3)
A25s4	5.63	1.60	3.13	5.98(5)	1.72(7)	9.69(−3)	3.28(−3)
B25s0	2.65	0.970	1.64	4.99(5)	1.20(7)	7.52(−4)	4.16(−4)
B25s4	12.1	4.80	12.7	8.03(5)	2.31(7)	4.08(−3)	6.22(−4)
C25s0	0.0466	0.0829	0.08	9.36(3)	2.13(5)	7.21(−6)	4.14(−6)
C25s4	6.73	2.94	5.77	5.77(5)	1.53(7)	1.23(−3)	1.69(−4)
C25s4b[h]	16.4	7.15	23.1	8.02(5)	2.10(7)	1.27(−3)	1.82(−4)
C25s5	13.5	5.73	16.5	8.27(5)	2.26(7)	3.83(−3)	4.94(−4)
C25s5b[h]	20.3	8.67	31.8	1.01(6)	2.74(7)	3.75(−3)	4.85(−4)
D25s0	0.166	0.0866	6.31	9.61(2)	2.24(4)	8.28(−7)	4.67(−7)
D25s4	0.804	0.354	14.0	1.39(5)	3.38(6)	1.05(−4)	3.81(−5)
D25s4b[h]	2.29	1.048	16.5	3.85(5)	8.60(6)	1.06(−4)	3.96(−5)
D25s6	19.2	7.78	33.5	6.77(5)	2.03(7)	4.57(−3)	2.68(−4)
D25s6b[h]	24.6	10.0	48.5	9.77(5)	2.76(7)	4.44(−3)	3.11(−4)
A40s4	7.76	2.00	4.05	3.77(5)	1.42(7)	1.23(−2)	5.29(−4)
B40s4	12.1	4.12	10.6	6.38(5)	2.13(7)	3.31(−3)	1.06(−4)
C40s4	11.6	4.67	10.4	6.12(5)	1.97(7)	2.70(−3)	1.93(−5)

Notes. [a]The A-series models have metallicity of $Z = Z_\odot$, B-series $Z = 10^{-1}$, C-series $Z = 10^{-5}$ and D-series $Z = 10^{-7}$.
[b]Central neutron exposure calculated according to equation (2).
[c]Neutron exposure averaged over He-core (see equation 3).
[d]Number of neutron captures per seed calculated according to equation (4), averaged over the He-core mass.
[e]Maximum of the mean neutron density.
[f]Maximum of the central neutron density.
[g]Values in parentheses are the exponents ($x(y) = x \times 10^y$).
[h]This model was calculated with the same initial parameters as the model, on the line above, but with $^{17}O(\alpha, \gamma)$ reaction rate of CF88 divided by 10.

(i) Because only a small helium mass fraction, $X(^4He)$, is left when $^{22}Ne+\alpha$ is activated (less than 10 per cent in mass fraction), the competition with other α-captures as the $^{12}C(\alpha, \gamma)$ and 3α is essential at the end of He-burning and will affect the *s*-process efficiency in core He-burning.

(ii) The low amount of $X(^4He)$, when the neutron source is activated, means also that not all of ^{22}Ne is burned and a part of it will be left for subsequent C-burning phase. This depends on the stellar core size. The more massive the core, the more ^{22}Ne is burned and the more efficient is the *s*-process in core He-burning, as can be seen from the increasing number of neutron captures per seed n_c from 0.77, 2.42, 3.13 and 4.05 for the four models mentioned before, which have M_{CO} of 2.35, 5.53, 6.97 and 15.04 $M_\odot$, respectively (see Table 2). This is a well-known behaviour already found in previous works (Prantzos et al. 1990; Baraffe et al. 1992; Baraffe & Takahashi 1993; Rayet & Hashimoto 2000; The et al. 2000, 2007; Pumo et al. 2010).

(iii) During the late He-burning stages, the bulk of the core matter consists of ^{12}C and ^{16}O, which are both strong neutron absorbers. They capture neutrons to produce ^{13}C and ^{17}O, respectively. ^{13}C will immediately recycle neutrons via $^{13}C(\alpha, n)$ in He-burning conditions. Instead, we have seen that the relevance of ^{16}O as a neutron poison depends on the $^{17}O(\alpha, \gamma)$ and $^{17}O(\alpha, n)$ rates. In particular, the strength of primary neutron poisons like ^{16}O increases towards lower metallicities, because of the decreasing ratio of seeds to neutron poisons.

The *s*-process production in the non-rotating models is shown in Figs 6 ($Z = Z_\odot$), 7 ($Z = 10^{-3}$), 8 ($Z = 10^{-5}$) and 9 ($Z = 10^{-7}$). In combination with the values given in Table 4, we can see that the models confirm the trends expected for the *s*-process in non-rotating massive stars, which we will call the *standard s*-process in the rest of this paper. The production of nuclei between $A = 60$ and 90 decreases with decreasing metallicity and mass. The decreasing production with decreasing metallicity is due to the secondary nature of both the neutron source ($^{22}Ne(\alpha, n)^{25}Mg$) and the seeds (mainly iron; see e.g. Prantzos, Hashimoto & Nomoto 1990; Raiteri, Gallino & Busso 1992; Pignatari & Gallino 2008). During helium burning, the neutron poisons are a mixture of secondary (mainly ^{20}Ne, ^{22}Ne and ^{25}Mg) and primary (mainly ^{16}O) elements.

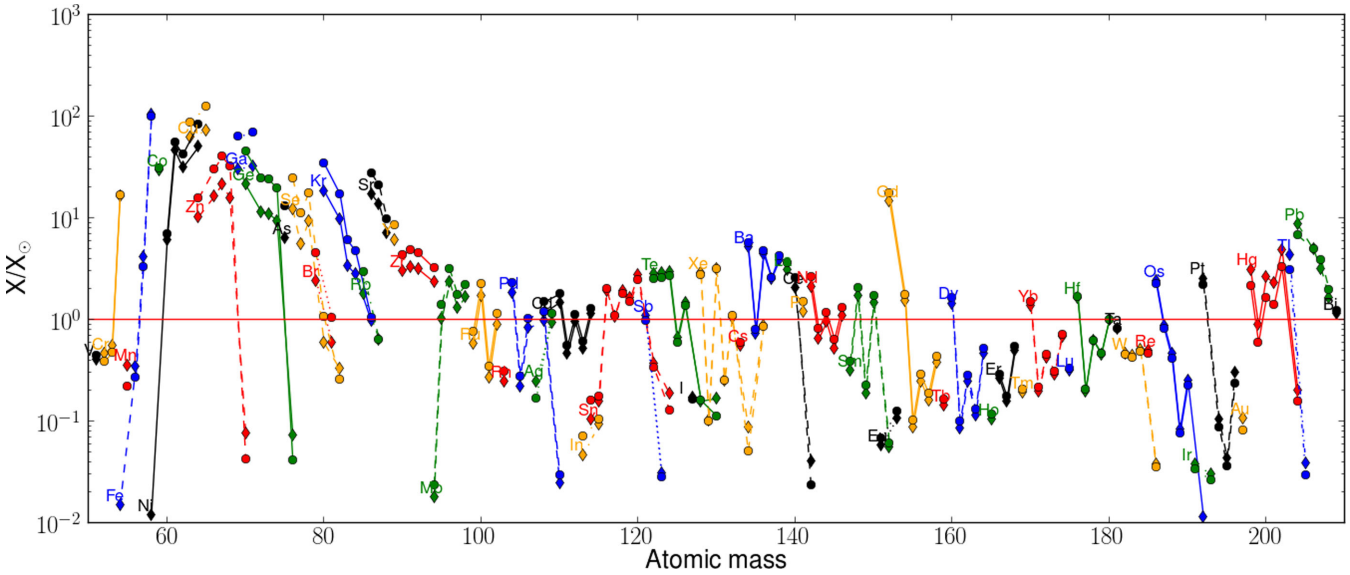

Figure 6. Isotopic overproduction factors (abundances over initial abundances) of 25 $M_\odot$ models with solar metallicity after He exhaustion. The rotating model (A25s4, circles) has slightly higher factors than the non-rotating model (A25s0, diamonds).

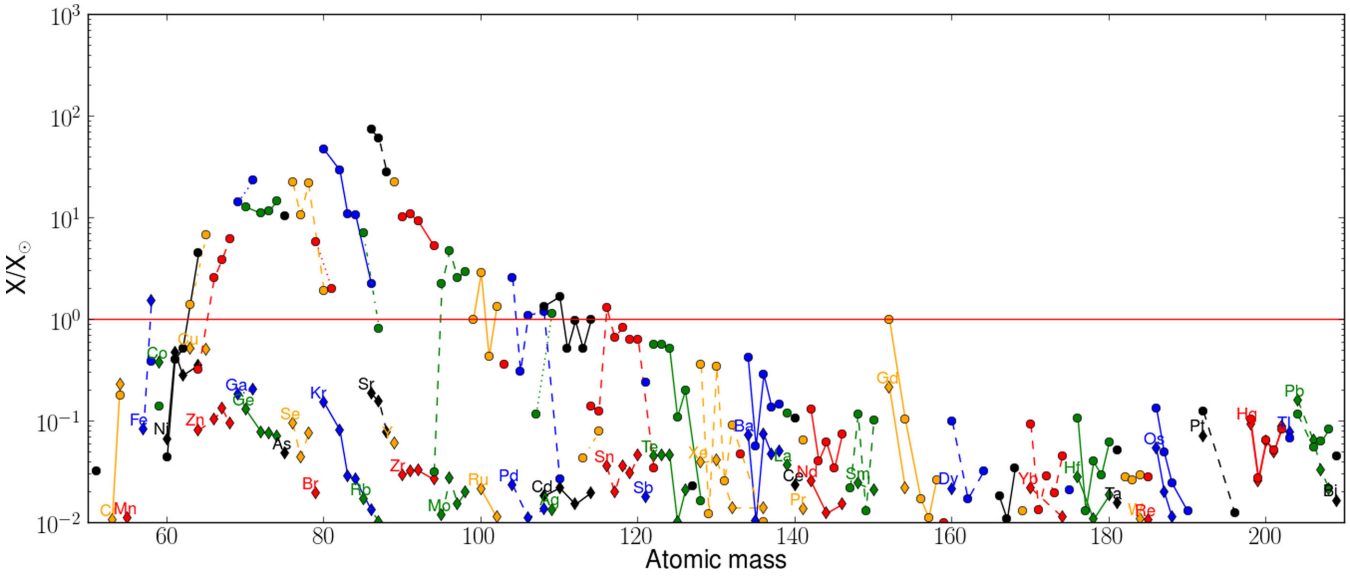

Figure 7. Isotopic abundances normalized to solar abundances of 25 $M_\odot$ models with $Z = 10^{-3}$ after He exhaustion. The rotating model (B25s4, circles) has higher factors than the non-rotating model (B25s0, diamonds).

The *s*-process production thus becomes negligible below $Z/Z_\odot = 10^{-2}$ (Prantzos et al. 1990), which we confirm with our non-rotating models at $Z = 10^{-5}$ and 10^{-7} (C and D series). The decreasing production with decreasing mass is due to the fact that lower mass stars reach lower temperature at the end of He-burning. Thus, less ^{22}Ne is burnt during He-burning (see Table 4).

The only model that does not follow this trend is the very low metallicity model D25s0. It shows a higher *s*-process efficiency than C25s0. This model has a smooth transition between central H- and He-burning. When small fractions of hydrogen are still present in the core, temperatures of $T_8 = 1.4$ are reached and the 3α-reaction is already activated. It leads to the immediate transformation of the ^{12}C produced into ^{14}N by ^{12}C(p, γ)^{13}N(β^+)^{13}C(p, γ)^{14}N (Baraffe et al. 1992) and therefore also the consumption of the remaining protons. In this way, $X(^{22}\mathrm{Ne}) = 1.2 \times 10^{-6}$ of primary ^{22}Ne is produced. Still as for non-rotating $Z = 10^{-5}$ models, D25s0 produces negligible amounts of heavy elements. This model shows a behaviour a bit similar to Pop III (metal-free) stars, which cannot produce enough energy by the pp-chains and therefore go into a state of combined hydrogen and weak He-burning, producing non-negligible amounts of primary ^{14}N as in previous studies (Ekström et al. 2008; Heger & Woosley 2010).

4.2 He-shell burning

Shell He-burning, similarly to the other burning shells, appears at higher temperatures and lower densities than the equivalent central burning phase. In our models, high-temperature conditions of $T_8 \approx 3.5$–4.5 and $\rho \approx 3$–5.5×10^3 g cm^{-3} cause an efficient ^{22}Ne(α,n) activation for the *s*-process in shell He-burning. However, the

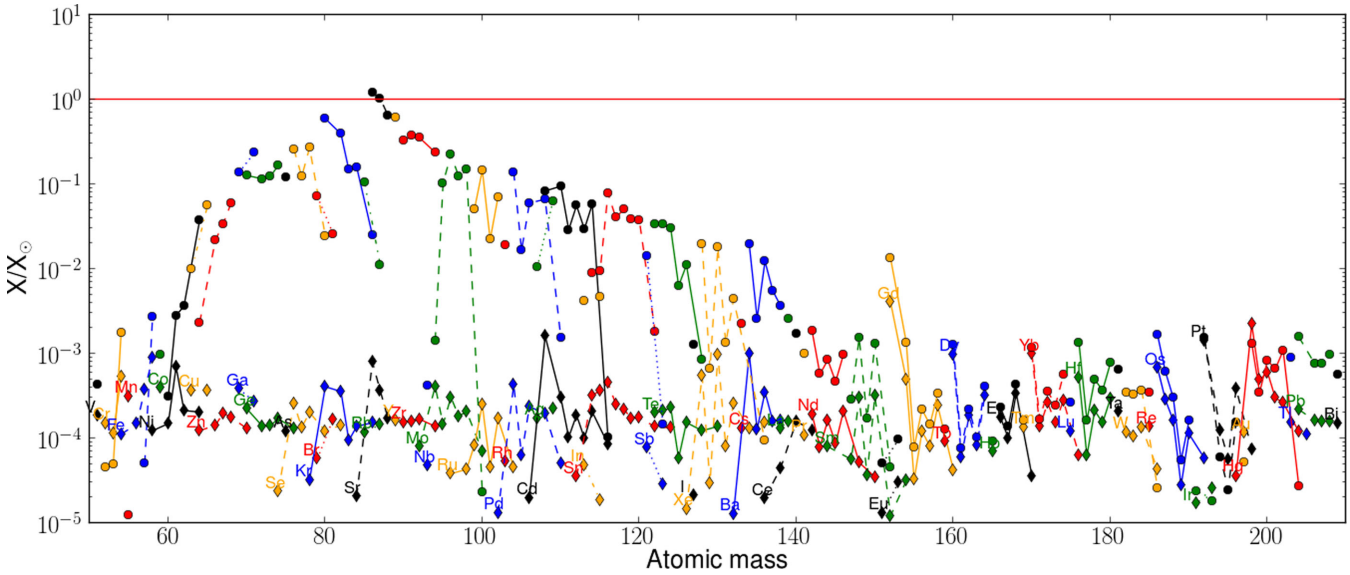

Figure 8. Isotopic abundances normalized to solar abundances of 25 $M_\odot$ models with $Z = 10^{-5}$ after He exhaustion. The rotating model (C25s5, circles) has much higher factors than the non-rotating model (C25s0, diamonds).

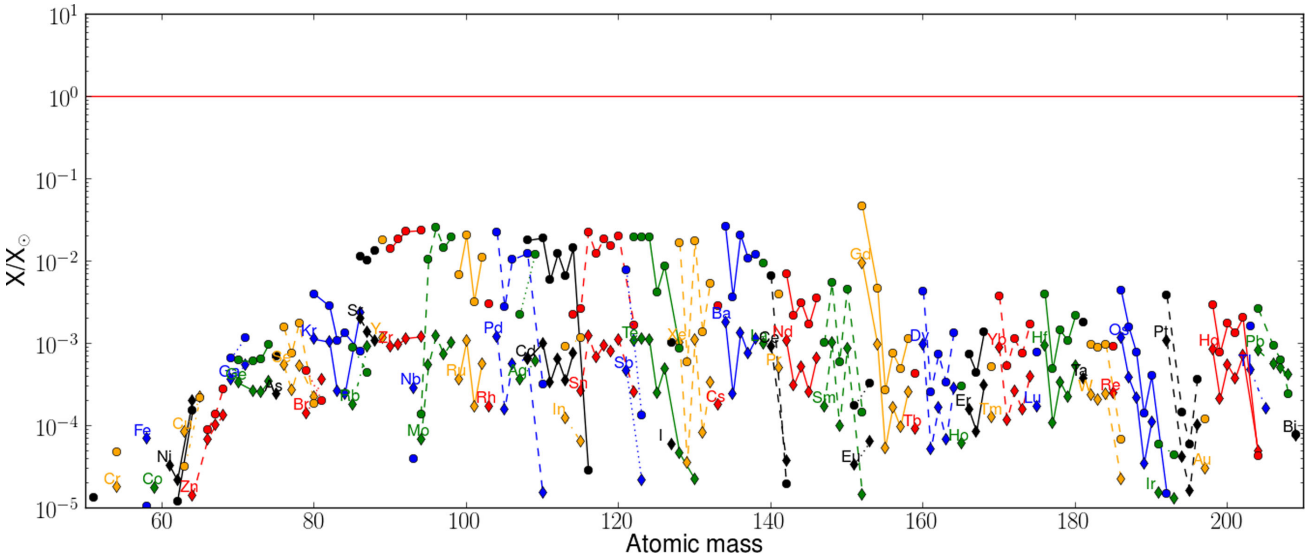

Figure 9. Isotopic abundances normalized to solar abundances of 25 $M_\odot$ models with $Z = 10^{-7}$ after He exhaustion. The rotating model (D25s6, circles) has slightly higher factors than the non-rotating model (D25s0, diamonds).

highest neutron densities are reached in all our models only in the layers below the convective shell helium burning. Therefore, only a narrow mass range, extending over about 0.2 $M_\odot$ in non-rotating models, at the bottom of the He-shell is strongly affected by neutron capture nucleosynthesis. The contribution of the *s*-process in the He-shell amounts to at most ∼5 per cent of the total *s*-process yields for the solar metallicity 25 $M_\odot$ model. For less massive stars, the He-shell gains more weight and produces in 15 $M_\odot$ models with rotation up to 50 per cent of the total *s*-process rich SN ejecta. Thus, according to our models for the 15–20 $M_\odot$ stars, the He-shell *s*-process contribution has to be considered (see also Tur et al. 2009).

4.3 C-shell burning

Shell C-burning occurs in the CO-core (see Table 2) after central C-burning. Temperatures and densities at the start of C-shell burning show the same trend with stellar mass as the core burning conditions, i.e. the temperature increases and the density decreases with stellar mass. They vary between $T_9 \approx 0.8$, $\rho \approx 2 \times 10^5$ g cm^{-3} in 15 $M_\odot$ models and $T_9 \approx 1.3$, $\rho \approx 8 \times 10^4$ g cm^{-3} in 40 $M_\odot$ models. These temperatures are higher than in the central C-burning, where $T_9 = 0.6$–0.8.

The efficiency of the *s*-process mainly depends on the remaining iron seeds and ^{22}Ne left after He-burning, $X_r(^{22}\mathrm{Ne})$, in the CO-core. All the remaining ^{22}Ne is burned quickly with maximal neutron densities between 6×10^9 and 10^{12} cm^{-3}, for the two extremes in models B15s4 and A40s4, respectively. The time-scale of this *s*-process is in our models of the order of a few tens of years in 15 $M_\odot$ stars to a few tenth of a year in 40 $M_\odot$.

A striking difference between the *s*-process in the He-shell and in the C-shell is the neutron density, which is much higher in the C-shell than in the He-shell. The activation of ^{22}Ne(α, n) at the start

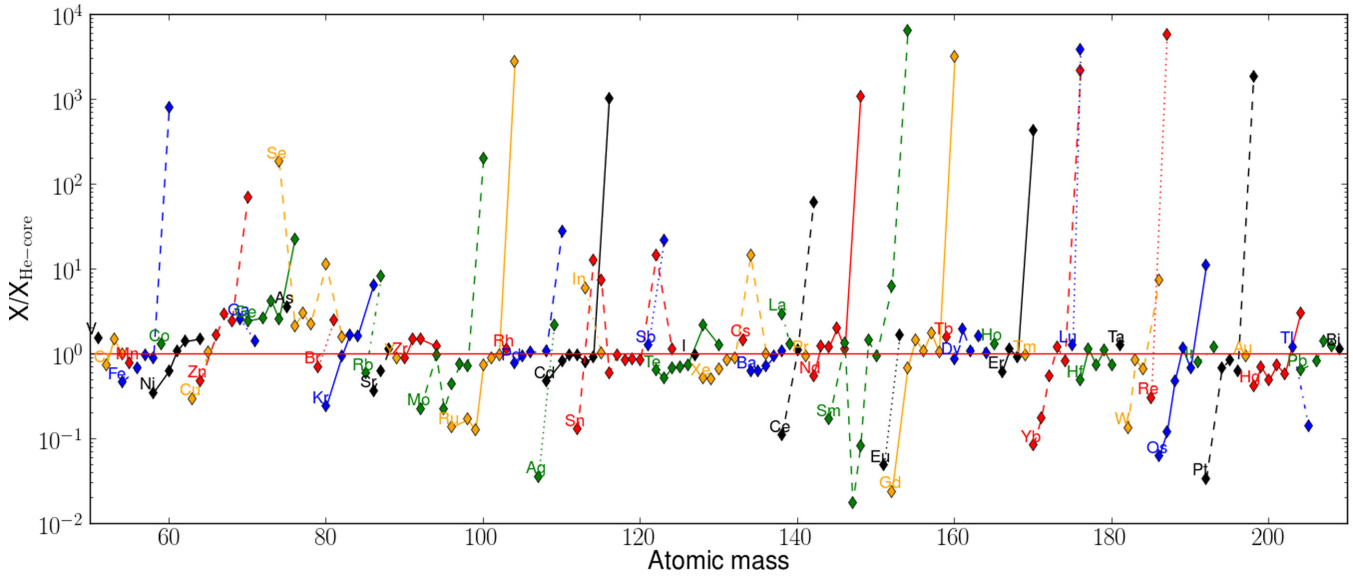

Figure 10. Ratio of abundances after shell C-burning to the abundances after core He-burning, X_C/X_{He}, in a non-rotating 25 $M_\odot$ star at $Z = Z_\odot$ (A25S0). It illustrates the modification of the abundances by *s*-process in shell C-burning.

of C-shell burning leads to a short neutron burst with relatively high neutron densities (typically $n_n \sim 10^{10}$–10^{12} cm^{-3}, see The et al. 2000, 2007), compared to He-burning ($n_n \sim 10^5$–10^7 cm^{-3}, see Table 4 and references above).

This leads to a different *s*-process nucleosynthesis than during the He-shell burning. The ratio of abundances after shell C-burning to the abundances after core He-burning, X_C/X_{He}, is plotted for the non-rotating 25 $M_\odot$ model at $Z = Z_\odot$ in Fig. 10. We can see an overproduction of most isotopes from Zn to Rb. The overproduction during C-burning shell is also found in models of other initial mass, which have both

(i) $X_r(^{22}Ne) \gtrsim 10^{-3}$ and
(ii) $X(^{56}Fe) \gtrsim 10^{-4}$, at the start of shell C-burning.

Therefore, in these calculations only 15–25 $M_\odot$ stars at solar Z have a strong C-shell contribution in terms of neutron exposure.

In the mass range $A = 60$–90, there are several branching points at ^{63}Ni, ^{79}Se and ^{85}Kr, respectively. The high neutron densities modify the *s*-process branching ratios, in a way that the neutron captures on the branching nuclei are favoured over the beta-decay channel (see e.g. Pignatari et al. 2010, and references therein). As a consequence of this, isotopic ratios like ^{63}Cu/^{65}Cu, ^{64}Zn/^{66}Zn, ^{80}Kr/^{82}Kr, ^{79}Br/^{81}Br, ^{85}Rb/^{87}Rb and ^{86}Sr/^{88}Sr are lowered. Overall, stars with different initial masses show very different final branching ratios. For instance, stars with 15 $M_\odot$ and with 20 $M_\odot$ (without rotation) produce ^{64}Zn, ^{80}Kr, ^{86}Sr in the C-shell, while in heavier stars these isotopes are reduced compared to the previous He-core.

The impact of the high neutron densities during C-shell can be seen in Fig. 10. It causes up to three orders of magnitude overproduction of some *r*-process nuclei, such as ^{70}Zn, ^{76}Ge, ^{82}Se or ^{96}Zr, compared to the yields of the 'slower' *s*-process during He-burning. However, the production of *r*-only nuclei in carbon burning compensates only the destruction in the He-core *s*-process when looking at the final yields. Only for the 40 $M_\odot$ model is ^{96}Zr weakly produced.

During C-burning, the main neutron poisons are ^{16}O, ^{20}Ne, ^{23}Na and ^{24}Mg, which are all primary. Thus, the C-shell contribution to the *s*-process will vanish at low metallicities even faster than during He-burning. In our non-rotating stellar models with $Z < Z_\odot$, the C-burning shell has a small contribution (<10 per cent).

Many aspects of this phase depend on the rates of a few key nuclear reactions. First, how the shells proceed depends on whether central C-burning takes place in a radiative or a convective core. It is thus sensitive to the C/O ratio in the core after He-burning and therefore to the ^{12}C(α, γ) rate. The uncertainty of this rate and its impact on the stellar structure evolution were studied for example in Imbriani et al. (2001), El Eid, Meyer & The (2004) and Tur et al. (2009). In our models, between one and three convective C-burning shells appear in the course of the evolution. The last shell has a maximal extension up to $M_r = M_C^{max}$ (given in Table 2). In most of the models, a large fraction of the He-burning *s*-process material is reprocessed (e.g. Pignatari et al. 2010). Indeed, comparing M_C^{max} to M_{He}^{max} in Table 2 shows that only 10–20 per cent of the CO-core is not reprocessed and keeps the pure signature of the He-burning *s*-process.

Secondly, the *s*-process nucleosynthesis depends on the number of free α particles present in the shell that can trigger neutron production by ^{22}Ne(α, n) (Raiteri et al. 1991b) or ^{13}C(α,n) (Bennett et al. 2012; Pignatari et al. 2013). In carbon burning, α particles are released by the ^{12}C+^{12}C α-channel. The following studies by Limongi, Straniero & Chieffi (2000), Rauscher et al. (2002), The et al. (2007) and Pignatari et al. (2010) confirmed that ^{22}Ne(α, n) is the only important neutron source in C-shell burning, where the remaining ^{22}Ne left after central He-burning is consumed in a very short time (time-scale ~1 yr). At shell C-burning temperatures ($T_9 \sim 1$), the ratio of the ^{22}Ne(α, n) to ^{22}Ne(α, γ) rates is about 230. In these conditions, the main competitor is the ^{22}Ne(p, γ), where protons are made by the C-fusion channel ^{12}C(^{12}C,p)^{23}Na. Alternatively, Bennett et al. (2012) and Pignatari et al. (2013) showed that for ^{12}C+^{12}C larger than about a factor of 100 compared to the CF88 rate at typical central C-burning temperatures, the ^{13}C(α,n)^{16}O reaction activated in the C core may strongly affect the final *s*-process yields. The ^{12}C+^{12}C rate needs to be better constrained by experiments (e.g. Wiescher, Käppeler & Langanke 2012). Other neutron sources as ^{17}O(α, n) and ^{21}Ne(α, n) recycle most of the

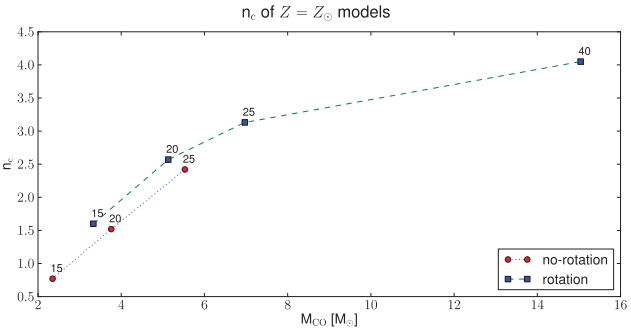

Figure 11. Average number of neutron captures per seed n_c versus M_{CO} for solar metallicity models after central He-burning. Blue squares show rotating stars and red circles non-rotating stars. The initial mass of each star is written above the symbol.

neutrons absorbed by ^{16}O and ^{20}Ne, respectively (e.g. Limongi et al. 2000).

5 IMPACT OF ROTATION ON THE *s*-PROCESS

5.1 Impact during the various burning stages

Rotation significantly changes the structure and pre-SN evolution of massive stars (Hirschi et al. 2004) and thus also the *s*-process production. Rotating stars have central properties similar to more massive non-rotating stars. In particular, they have more massive helium burning and CO-cores (see Table 2), respectively, which is an effect of rotation also found by other studies (e.g. Heger & Langer 2000; Chieffi & Limongi 2013). Our models with rotation show typically 30–50 per cent larger He-cores and CO-cores than the non-rotating models. A 20 $M_\odot$ star with rotation has thus a core size which is almost as large as the one of a 25 $M_\odot$ non-rotating star. The higher core size means higher central temperatures at the same evolutionary stage and consequently the ^{22}Ne+α is activated earlier. In these conditions, the He-core *s*-process contribution increases at the expense of the C-shell contribution. Since in He-burning conditions the amount of neutrons captured by light neutron poisons and not used for the *s*-process is lower compared to C-burning conditions, an overall increase of the *s*-process efficiency is obtained (see also Pignatari et al. 2010).

At solar metallicity the difference between rotating and non-rotating stars is mainly found in the core size, but not in the amount of available ^{22}Ne. This becomes clear if one compares $X(^{22}\mathrm{Ne}) = \Delta X(^{22}\mathrm{Ne}) + X_\mathrm{r}(^{22}\mathrm{Ne})$ of the A-series models in Table 4. In mass fraction, $X(^{22}\mathrm{Ne}) \approx 1.3 \times 10^{-2}$ is available for α-captures, which is therefore mainly secondary. Similar values are obtained in both rotating and non-rotating models. The difference in *s*-process efficiency is therefore mainly due to the rotation-induced larger core size and the related impact on temperature (higher) and density (lower). The difference in the neutron exposure is due to higher fraction of burned ^{22}Ne. The difference in *s*-processing between rotating and non-rotating stars is the smallest at 25 $M_\odot$ (A25s0 versus A25s4), when comparing 15 to 25 $M_\odot$ models. It is related to the saturation of the *s*-process towards higher core/initial masses, which was already found by Langer, Arcoragi & Arnould (1989) and can be seen in Fig. 11. This figure shows n_c after He-burning versus CO-core mass of rotating (blue squares) and non-rotating stars (red circles). We see that n_c saturates for $M_{CO} > 7\,M_\odot$ (initial mass >25 $M_\odot$). The saturation is caused by the exhaustion of ^{22}Ne. Typically, the model A40s4 has burned 96 per cent of available ^{22}Ne after He-burning.

In Fig. 6, the overproduction factors of 25 $M_\odot$ models (A25s0 and A25s4) with solar metallicity after the end of He-burning are shown. Model A25s4 (circles) shows only a moderate increase of the *s*-process production with respect to A25s0 (diamonds). Both models produce heavy isotopes from iron seeds up to the Sr-peak ($A \approx 90$). In A25s0 model, 66 per cent of Fe is destroyed, and in A25s4 73 per cent. The varying overproduction factors ($\neq$1) beyond $A = 90$ are the signature of a local redistribution of pre-existing heavy nuclei. This figure therefore illustrates that not only the *s*-process quantities given in Table 4 are similar, but also the abundance patterns of rotating and non-rotating models at solar *Z* are almost identical. The difference in the efficiency is mostly caused by the larger core size in the rotating models.

At sub-solar metallicities, the differences between rotating and non-rotating models are much more striking. Rotating models have much higher neutron exposures compared to non-rotating stars, which is due to the primary ^{22}Ne produced and burned during central He-burning (see Section 3). This is also illustrated by the 3–270 times higher amount of ^{22}Ne burned in rotating stars up to central He exhaustion, depending on the initial mass (or M_{CO}) and metallicity. The large production of neutrons by ^{22}Ne is partially compensated by the larger concentration of ^{25}Mg and ^{22}Ne itself, which become primary neutron poisons in rotating massive stars (Pignatari et al. 2008). Figs 7, 8 and 9 show the abundance normalized to solar in the CO-core of 25 $M_\odot$ stars with $Z = 10^{-3}$, 10^{-5} and 10^{-7} just after central He exhaustion, each for a rotating (circles) and a non-rotating model (diamonds). Going from $Z = Z_\odot$ (Fig. 6) to $Z = 10^{-3}$ and 10^{-5} (Figs 7 and 8), the production of nuclei between $A = 60$ and 90 vanishes in the non-rotating models, which is what is expected from the combination of secondary neutron source, secondary seeds and primary neutron poisons. The non-rotating model at $Z = 10^{-7}$ (D25s0, diamonds in Fig. 9) is special with its small amount of primary ^{22}Ne. The rotating models at sub-solar *Z* produce efficiently up to Sr ($Z = 10^{-3}$), Ba ($Z = 10^{-5}$) and finally up to Pb ($Z = 10^{-7}$). At the same time, the consumption of iron seeds increases from 74 per cent at $Z = Z_\odot$ (A25s4) to 96 per cent (B25s4), 97 per cent (C25s4) and 99 per cent (D25s6) at $Z = 10^{-3}$, 10^{-5} and 10^{-7}, respectively. Also with the standard rotation rate $\upsilon_\mathrm{ini}/\upsilon_\mathrm{crit} = 0.4$ around 90 per cent of initial Fe is destroyed in models with 25 $M_\odot$ and $Z < Z_\odot$. Hence, already from the *s*-process in He-burning, one can conclude that the primary neutron source in the rotating models is sufficient to deplete all the seeds and the production is limited by the seeds (not the neutron source any more). The other stellar masses show similar trends with *Z*. It is interesting to look at the rotation dependence of the non-standard *s*-process production. At $Z = 10^{-5}$, the faster rotating model (C25s5) does not produce more heavy isotopes beyond iron compared to the one with standard rotation (C25s4). Instead, what happens is that not only iron is depleted but elements up to Sr are partially destroyed (after being produced) and heavier elements like Ba are produced. Even at the lowest metallicities in a very fast rotating model (D25s6 and D25s6b, $\upsilon_\mathrm{ini}/\upsilon_\mathrm{crit} = 0.6$ instead of the standard 0.4), and thus with a larger primary neutron source, there is no additional production of *s*-process elements starting from light element seeds like ^{22}Ne. Indeed, going from [Fe/H] = −3.8 (C25s4) to [Fe/H] = −5.8 (D25s4), the Sr yield decreases by a factor of ∼9, while the Ba yield increases by a factor of 5. Hence, the production is limited mainly by the iron seeds.

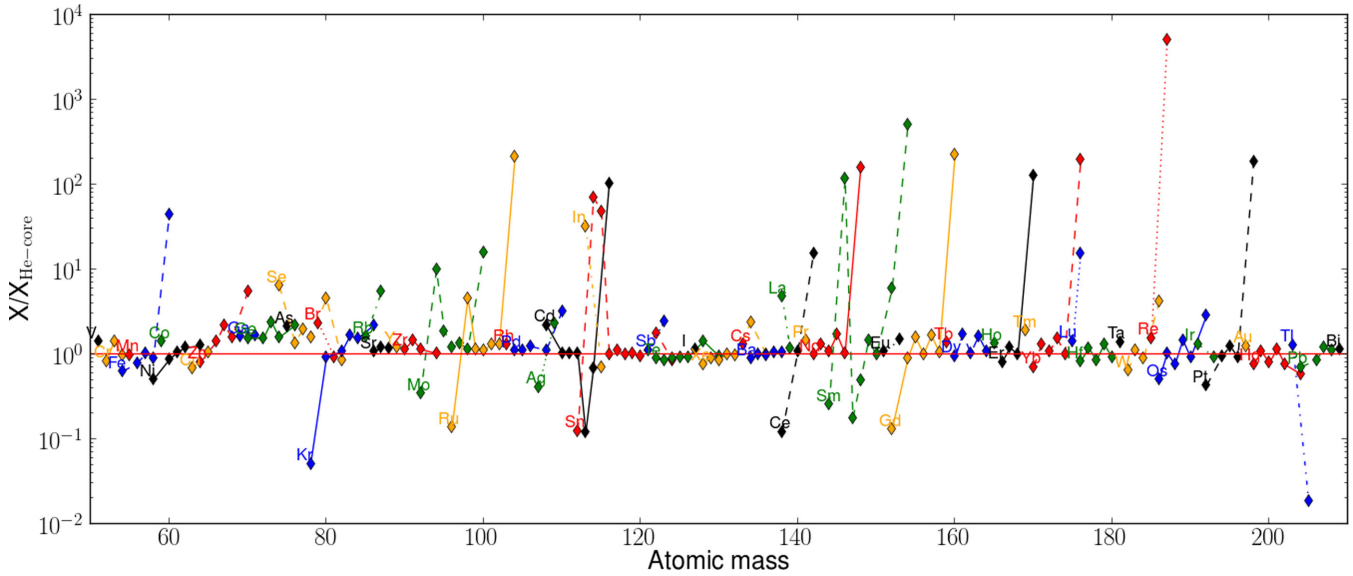

Figure 12. Ratio of abundances after shell C-burning to the abundances after core He-burning, X_C/X_{He}, in a rotating 25 $M_\odot$ star at $Z = Z_\odot$ (A25S4). It illustrates the modification of the abundances by *s*-process in shell C-burning.

Models with a reduced $^{17}O(\alpha, \gamma)$ (C25s4b, C25s5b, D25s4b and D25s6b) produce more neutrons. Actually, reducing this rate has similar consequences to increasing the amount of ^{22}Ne. Already a reduction of $^{17}O(\alpha, \gamma)$ by a factor of 10 boosts the *s*-process up to Ba more (model C25s4b) than going from standard (C25s4) to faster rotation (C25s5). Models C25s4b, C25s5b, D25s4b and D25s6b show [Sr/Ba] of about +1, +0.3, 0 and −0.6. These models therefore emphasize the importance of ^{16}O as a neutron poison, as discussed in Frischknecht et al. (2012). Note that the models with a reduced $^{17}O(\alpha, \gamma)$ are still limited by seeds.

The normalization to solar composition allows one to compare the low-*Z* models in Figs 7–9 to the solar *Z* models in Fig. 6 with respect to their total production. Model B25s4 produces overall similar amounts of heavy nuclei in the range $A = 60$–90 as models A25s0 and A25s4. A closer look reveals that the solar metallicity models produce higher amounts beyond Fe up to Ge. For isotopes of As, Se, Br and Kr, A25s0, A25s4 and B25s4 produce similar amounts, while for Sr, Y and Zr B25s4 produces more. However, here one has to keep in mind that for the final picture also the shell C-burning contribution has to be taken into account. The impact on GCE of these results has been discussed elsewhere (e.g. Cescutti et al. 2013). However, according to models A25s0, A25s4 and B25s4 compared to C25s5 (Fig. 8), rotating stars at $Z = 10^{-5}$ (initial [Fe/H] = −3.8) probably do not contribute significantly to the *s*-process chemical enrichment at solar *Z*, because the $X/X_\odot$ values are only around 1 or lower for C25s5. This is confirmed for the model D25s6 in Fig. 9. For the Sr, Y and Zr, a small contribution from rotating stars with *Z* between 10^{-3} (initial [Fe/H] = −1.8) and 10^{-5} can nevertheless be expected. Instead, for the non-rotating stars, the *s*-process contribution is already negligible at 10^{-3}.

Rotation only has a mild impact on the He-shell contribution. Rotation-induced mixing widens the radiative zone where $^{22}Ne(\alpha, n)$ is activated to about 0.4 $M_\odot$ in rotating stars (compared to 0.2 $M_\odot$ in non-rotating models). As explained in the previous section, the contribution to the total *s*-process yields is therefore low in our models, and only in the region of 5 per cent for solar metallicity 25 $M_\odot$ stars with and without rotation. For less massive stars, the He-shell gains more weight and produces in 15 $M_\odot$ models with rotation up to 50 per cent of the total yields.

In Fig. 12, the ratio of abundances after shell C-burning to the abundances after core He-burning, X_C/X_{He}, is plotted for the rotating 25 $M_\odot$ model at $Z = Z_\odot$ (A25s4). As in the non-rotating $Z = Z_\odot$ model, the high neutron densities lower the *s*-process branching ratios. Rotating models with 15 $M_\odot$ still produce ^{64}Zn, ^{80}Kr, ^{86}Sr in the C-shell, while in 20 $M_\odot$ and heavier stars these isotopes are depleted due to the large neutron densities favouring the neutron capture channel at the *s*-process branching points ^{63}Ni, ^{79}Se and ^{85}Kr (e.g. Pignatari et al. 2010). This effect mainly occurs at solar *Z* (or higher), but it is still relevant also at lower metallicities to calculate the complete *s*-process pattern.

5.2 Relative contributions and total yields

In Fig. 13, the yields of ^{68}Zn of the three *s*-process sites normalized to the total yields are displayed, for non-rotating stars on the left-hand side and rotating stars on the right-hand side, and from top to the bottom for He-core, C-shell and He-shell burning yields. We plotted ^{68}Zn as a representative for the isotopes in range $A = 60$–80, because it is produced by the *s*-process in all three phases. This figure allows us to compare the contributions of the three different sites to the total yields. The following points can be derived.

(i) In general, the contribution from He-core burning (colours yellow to red in Figs 13a and b) dominates over the other two phases overall.

(ii) Shell carbon burning is, compared to the other two sites, only efficient at solar metallicity (see Figs 13c and d). The weak contribution at low *Z* is due to the low amount of ^{22}Ne left, the smaller amount of seeds and the primary neutron poisons, which have an increased strength towards lower *Z* in C-shell conditions. The only mass–metallicity range for which the C-shell dominates is at solar *Z* with $M \lesssim 25\,M_\odot$ for non-rotating models and with $M \lesssim 20\,M_\odot$ for rotating models. Such a dominant contribution from C-shell was not seen in the previous literature (e.g. The et al. 2007). This may be due to the high $^{22}Ne(\alpha, \gamma)$ rate of NACRE, which is in

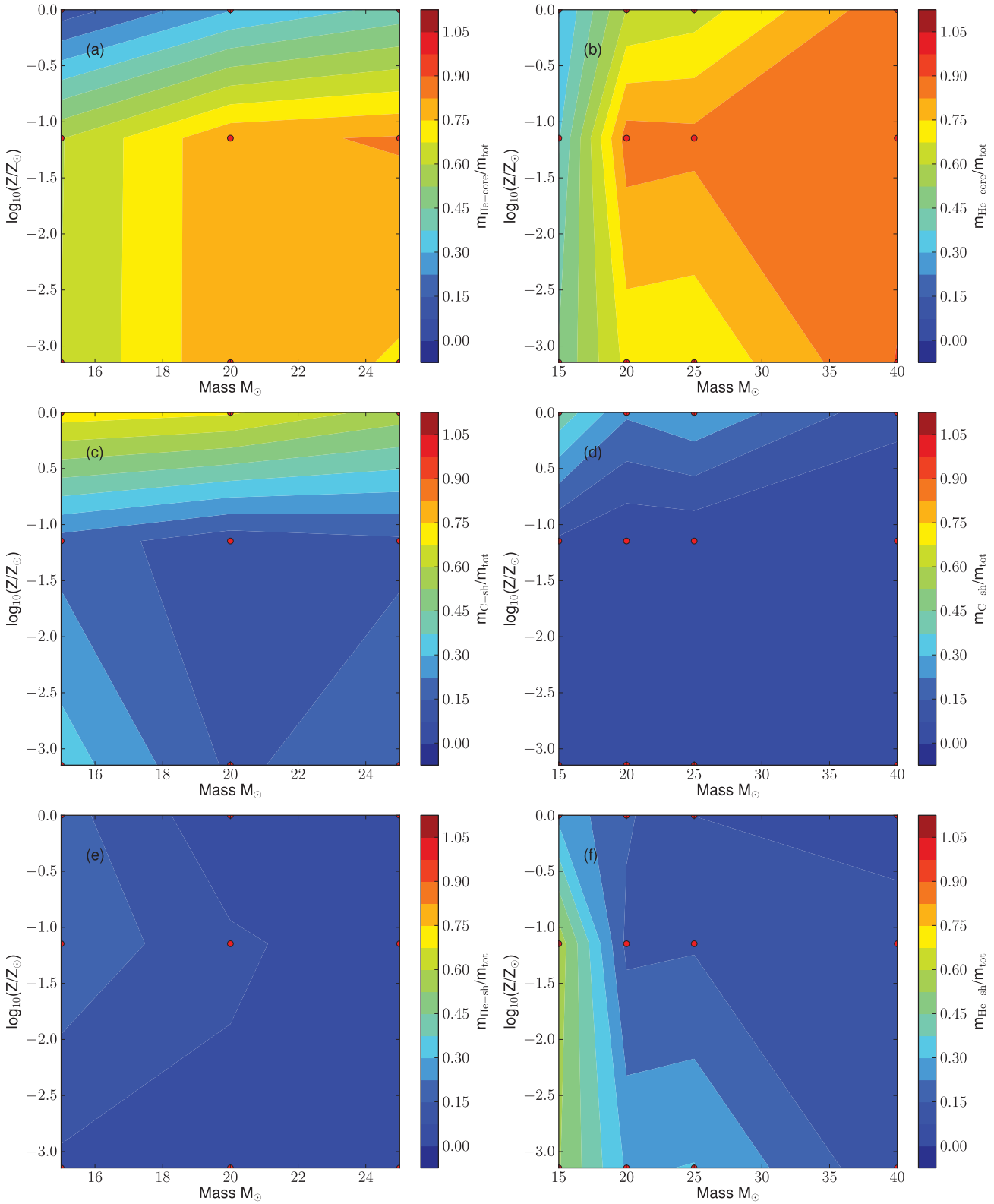

Figure 13. *s*-process site yields of ^{68}Zn normalized to the total yields to illustrate the different relative contributions as a function of mass and metallicity Z, for He-core without (a) and with rotation (b), for C-shell without rotation (c) and with rotation (d), and the He-shell without (e) and with rotation (f). The red circles display the location of our models in the mass–metallicity space. Note that decayed yields are plotted in this figure. The values in between the data points are interpolated linearly in $\log(m)$.

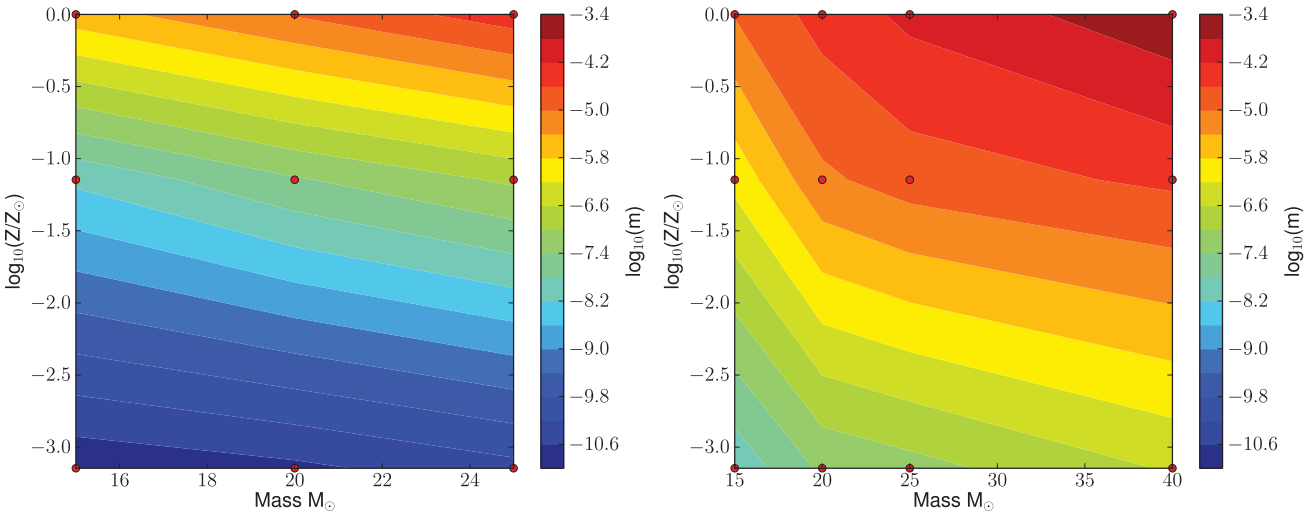

Figure 14. *s*-process yields, *m*, of ^{68}Zn in $M_\odot$ to illustrate the mass and metallicity dependence of the *s*-process, without rotation on the left-hand side and with rotation on the right-hand side. The red circles display the location of our models in the mass–metallicity space. The values in between the data points are interpolated linearly in log (*m*).

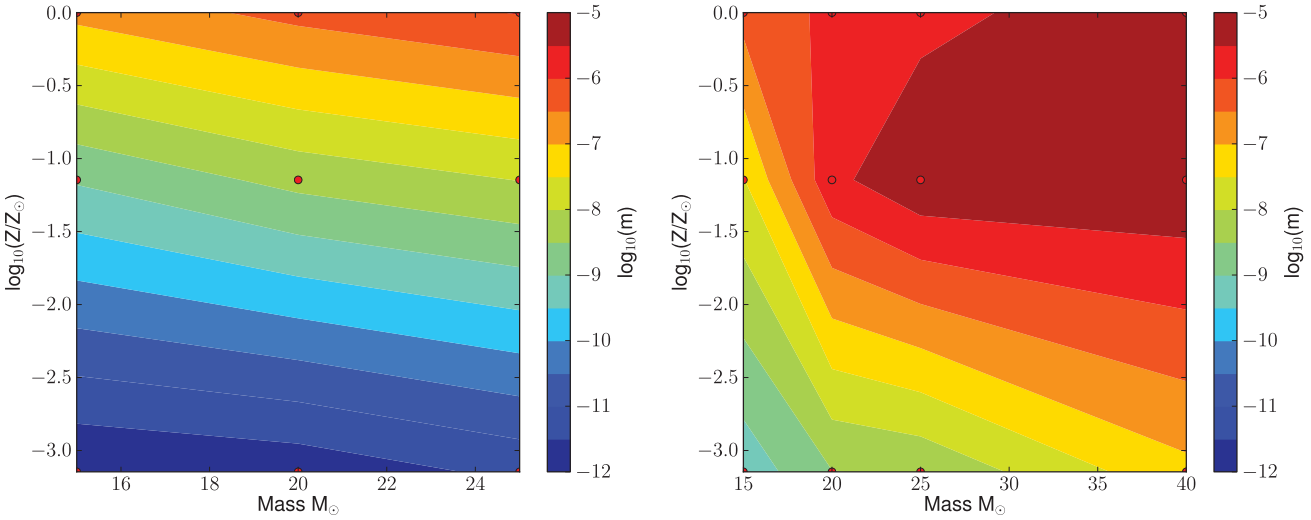

Figure 15. *s*-process yields, *m*, of ^{88}Sr in $M_\odot$ to illustrate the mass and metallicity dependence of the *s*-process, without rotation on the left-hand side and with rotation on the right-hand side. The red circles display the location of our models in the mass–metallicity space. The values in between the data points are interpolated linearly in log (*m*).

strong competition to the neutron source during central He-burning and dominates for stars with $M \lesssim 20\,M_\odot$. This inhibition during He-core burning is weaker for rotating stars since they have higher central temperatures.

(iii) Shell He-burning contributes only a small fraction but typically 5 per cent to the final yields (see Figs 13e and f). The exceptions are the rotating 15–25 $M_\odot$ stars at low *Z* and rotating 15–20 $M_\odot$ stars at solar *Z*. It is the effect of decreasing contribution from the He-core towards lower masses and the higher burning temperatures in the shell compared to the He-core, which allows an efficient activation of ^{22}Ne(α, n) in the 15 $M_\odot$ models. Additionally, the He-shell is not limited by the diminished iron seeds consumed by *s*-process in He-core but occurs in a region still containing its initial iron content. Note that decayed yields are plotted in this figure.

In Fig. 14, the dependence of total ^{68}Zn yields on the mass and metallicity is displayed for rotating stars with standard rotation rate ($\upsilon_{\rm ini}/\upsilon_{\rm crit} = 0.4$) on the right-hand side and for non-rotating stars on the left-hand side. The red circles display the location of our models in the mass–metallicity space. The values in between the data points are interpolated linearly in log (*m*). As mentioned above, ^{68}Zn is representative for the isotopes in range $A = 60$–80. A similar plot for the neutron-magic isotope ^{88}Sr is presented in Fig. 15 to show the dependence of the Sr-peak production on rotation (^{86}Sr, ^{87}Sr, ^{89}Y and ^{90}Zr show the same trends as ^{88}Sr). Several differences between the standard and rotation-boosted *s*-process can be seen.

(i) Rotating models clearly produce more *s*-process elements at all metallicities.

(ii) Whereas the *s*-process production in non-rotating model decreases steeply with metallicity (dependence steeper than linear; e.g. Pignatari & Gallino 2008), the ^{68}Zn yields of rotating stars show a secondary-like behaviour, going from reddish to bluish colours towards lower *Z*. While the ^{68}Zn yields of non-rotating stars drop by five orders of magnitude when the metallicity goes down by a

Table 5. Production factors[a] of 25 $M_\odot$ models after central He exhaustion[b].

Model	A25s0[c]	A25s4[c]	Pi10-1	Pi10-2	T07-25K	T07-25C	Ra91a
Isotope				Overproduction factors			
^{63}Cu	62.0	88.0	127	134	60.8	78.2	91.8
^{65}Cu	73.7	125	280	317	128	205	226.3
^{64}Zn	10.4	15.7	34.1	36.8	30.7	43.6	41.0
^{66}Zn	16.5	30.0	76.3	88.7	59.6	107	118.9
^{67}Zn	21.8	40.7	109	127	82.9	153	171.7
^{68}Zn	16.0	32.1	99.1	121	73.1	158	164.7
^{70}Zn	0.1	0.0	0.3	0.3	0.4	0.6	–
^{69}Ga	30.8	63.1	126	156	–	–	208.6
^{71}Ga	32.6	69.4	147	187	–	–	263.9
^{70}Ge	21.5	45.2	154	193	112	270	253.7
^{72}Ge	11.7	24.9	88.0	114	75.2	201	190.7
^{73}Ge	11.2	24.0	82.4	107	46.9	128	128.8
^{74}Ge	9.5	19.5	71.0	94.2	37.5	110	99.3
^{76}Ge	0.1	0.0	0.0	0.0	–	–	–
^{75}As	6.4	13.1	45.3	60.2	27.4	81.9	59.6
^{76}Se	12.3	24.6	99.4	133	78.2	241	212.2
^{77}Se	5.6	11.1	44.0	59.1	–	–	88.6
^{78}Se	9.3	17.6	67.4	91.7	–	–	108.9
^{80}Se	0.6	1.1	1.5	1.9	1.3	4.0	–
^{82}Se	0.3	0.3	0.1	0.1	–	–	–
^{79}Br	2.4	4.5	15.6	21.3	–	–	36.6
^{81}Br	0.6	1.0	15.4	21.1	–	–	–
^{80}Kr	18.7	34.6	169	232	183	618	480.7
^{82}Kr	9.8	17.4	79.1	108	77.9	277	210.3
^{83}Kr	3.4	6.0	25.9	35.5	–	–	63.0
^{84}Kr	2.8	4.7	22.0	29.9	–	–	52.6
^{86}Kr	1.0	1.1	0.7	0.8	2.6	5.7	–
^{85}Rb	1.8	2.9	14.8	20.0	–	–	28.6
^{87}Rb	0.6	0.6	0.8	0.8	1.3	3.0	–
^{86}Sr	17.5	27.8	79.9	107	60.7	232	147.3
^{87}Sr	13.8	21.1	68.8	91.4	50.4	190	129.2
^{88}Sr	7.2	9.9	21.5	26.8	14.9	45.3	34.8
^{89}Y	6.2	8.6	15.6	18.9	–	–	22.3
^{90}Zr	3.0	4.3	6.9	8.2	–	–	–
^{91}Zr	3.3	4.8	8.6	10.1	–	–	–
^{92}Zr	3.2	4.6	7.3	8.5	–	–	–
^{94}Zr	2.4	3.2	5.4	6.3	–	–	–

References. Pi10-*x* – model *x* from Pignatari et al. (2010), T07-25K/C – model 25K/C from The et al. (2007), Ra91a – Raiteri et al. (1991a).

Notes. [a]Production factors are defined as the mass fractions/abundances X normalized to the initial ones $X_{\rm ini}$. Since we have here $Z = Z_\odot$ models, the production factors are $X/X_\odot$.

[b]In our models, the overproduction factors are constant throughout the convective core (due to the very fast convective mixing) so our central values are directly comparable with the literature where the 'core-averaged' overproduction factors are reported.

[c]The other authors used the solar abundances of Anders & Grevesse (1989), but we used the one of Asplund et al. (2005).

factor of 10^3, the yields from rotating stars drop only by a factor of 10^3. The scaling with metallicity is less steep for rotating models.

(iii) Furthermore, the Sr-peak isotopes do not show a secondary behaviour for stars with rotation and $M > 15\,M_\odot$ in the metallicity range between solar ($\log(Z/Z_\odot) = 0$) and about one hundredth ($Z = 1.4 \times 10^{-4}$, $\log(Z/Z_\odot) = -2$) of solar metallicity, but they eject maximal absolute yields around one tenth of solar metallicity (dark red around $\log(Z/Z_\odot) = -1$) for 20–30 $M_\odot$ stars.

6 COMPARISON TO THE LITERATURE AND OBSERVATIONS

6.1 Comparison to the literature

In Table 5, the overproduction factors $X_i/X_{i,\,\rm ini}$ in the centre of solar metallicity 25 $M_\odot$ models after the end of central He-burning are presented. It shows $X_i/X_{i,\,\rm ini}$ for isotopes between Cu and Zr for the models with (A25s4) and without rotation (A25s0), as well as for models 1 and 2 from Pignatari et al. (2010), models 25K and 25C from The et al. (2007) which are based on stellar models of El Eid et al. (2004), and the model from Raiteri et al. (1991a).

First of all, the overproduction factors in Table 5 show a wide spread between the models. For Cu and Zn isotopes, the most efficient models (Pi10-2, T07-25C, Ra91a) produce four to seven times more than the least efficient model (A25s0). This difference becomes even more pronounced for heavier isotopes, e.g. ^{86}Sr, where the difference from the least efficient (A25s0) to the most efficient models (T07-25C, Ra91a) can exceed a factor of 20. Model Pi10-2 produces large amounts of Cu isotopes, while for heavier elements the production factors are lower than T07-25C and Ra91a results.

In Table 6, we show the characteristic *s*-process parameters of the same models. The central neutron exposure $\tau_{\rm c}$ and the

Table 6. *s*-process parameters in the centre of 25 $M_\odot$ stars after central He exhaustion.

Model	τ_c[a] (mb^{-1})	$\langle\tau\rangle$[b] (mb^{-1})	n_c[c]	$\bar{n}_{n,max}$[d] (10^5 cm^{-3})	$n_{n,c,max}$[e] (10^7 cm^{-3})	$\Delta X(^{22}Ne)$ ($\times10^{-2}$)	$X_r(^{22}Ne)$ ($\times10^{-2}$)
A25s0	3.80	0.133	2.34	5.85	1.56	0.77	0.51
A25s4	4.86	0.160	3.06	5.98	1.72	0.97	0.33
Pi10-1	–	0.197	4.95	11.4	3.22	1.03	1.14
Pi10-2	–	0.209	5.35	10.1	2.88	1.47	0.70
T07-25K	5.00	0.15	3.63	2.53	–	1.39[f]	0.78
T07-25C	5.43	0.30	5.14	1.95	–	1.19[f]	0.98
Ra91a	–	0.206	5.67	6.79	1.80	1.06	0.96

Notes. [a]Central neutron exposure calculated according to equation (2).
[b]Neutron exposure averaged over He-core (see equation 3).
[c]Number of neutron captures per seed calculated according to equation (4), averaged over the He-core mass.
[d]Maximum of the mean neutron density.
[e]Maximum of the central neutron density.
[f]Assuming for the secondary ^{22}Ne a mass fraction of $X(^{22}Ne) = 2.17 \times 10^{-2}$ at the start of He-burning as in Pignatari et al. (2010).

Table 7. Reaction rates used in 25 $M_\odot$ $Z = Z_\odot$ models.

Model	A25s0	A25s4	Pi10-1	Pi10-2	T07-25K	T07-25C	Ra91a
$^{22}Ne(\alpha, n)$	Ja01	Ja01	Ja01	NACRE	NACRE	CF88	CF88
$^{22}Ne(\alpha, \gamma)$	NACRE	NACRE	Ka06	NACRE	NACRE	K94	CF88
$^{12}C(\alpha, \gamma)$	Ku02	Ku02	CFHZ85	CFHZ85	Ku02	CF88	CFHZ85
n-captures	K0.3	K0.3	K0.3	K0.3	Be92	Be92	

References. Pi10-*x* – model *x* of Pignatari et al. (2010), T07-25K/C – model 25K/C of The et al. (2007), Ra91a – Raiteri et al. (1991a), Ja01 – Jaeger et al. (2001), NACRE – Angulo et al. (1999), CF88 – Caughlan & Fowler (1988), Ka06 – Karakas et al. (2006), K94 – Käppeler et al. (1994), Ku02 – Kunz et al. (2002), CFHZ85 – Caughlan et al. (1985), K0.3 – KADoNiS v0.3, Be92 – Beer, Voss & Winters (1992).

convective core-averaged neutron exposure $\langle\tau\rangle$ together with the average number of neutron captures per seed n_c describe the *s*-process efficiency. These *s*-process quantities show a similar picture as the overproduction factors in Table 5. The most efficient models are again Pi10-2 and T07-25C, Ra91a, and the least efficient model is A25s0.

There are several important differences between our models (A25s0, A25s4) and the others, namely in the initial composition and the nuclear reaction input, which explain the big differences. Here these differences are listed.

(i) We used for our models with solar-like composition the initial chemical composition from Asplund et al. (2005) with a metallicity $Z = 0.014$. The other authors used the solar composition from Anders & Grevesse (1989) with $Z \approx 0.019$. It means that in our models the secondary ^{22}Ne and the iron seeds are reduced by about 35 per cent. From a reduction of the ^{22}Ne neutron source and the seeds, a reduction of the *s*-process production is expected. However, if one uses a solar-like composition with lower *Z*, this is partially compensated in the overproduction factors by the normalization to the smaller initial abundances. It is only partially compensated, because the source and the seeds are reduced while the primary poisons not, and the standard *s*-process scales therefore less than secondary. The impact of a similar change, from Anders & Grevesse (1989) composition to the one of Lodders (2003) with $Z = 0.0149$, was investigated by Tur et al. (2009). They found that the change of initial composition can modify the final production factors by 0.2–0.5 dex for 25 $M_\odot$ stars. Since we used $Z = 0.014$ in our solar *Z* models, the reduction in the overproduction factors is even higher.

(ii) In Table 7, the sources of the reaction rates used in the works, compared here, are listed. The neutron source and the $^{22}Ne(\alpha, n)/^{22}Ne(\alpha, \gamma)$ ratio, respectively, of our models are only similar in Pi10-1, but they use the lower rate for $^{22}Ne(\alpha, \gamma)$ of Karakas et al. (2006), which is lower than the NACRE rate we used. The rates for the neutron source of CF88 and NACRE are both considerably higher (see discussion in NACRE and Jaeger et al. 2001). Therefore, all other models used more favourable combinations of $^{22}Ne+\alpha$ rates for the *s*-process. There is an indication that our choice of rates leads to a too weak *s*-process at solar metallicity, because most isotopes (except for copper) are less overproduced compared to ^{16}O (see Pignatari et al. 2010, for more details).

(iii) In the mass region $A = 50$–90, many (n, γ) rates, relevant for the *s*-process, were found to be lower by new measurements in the past 15 years. Thus, the neutron capture rates also changed over the time frame of the different studies. Pignatari et al. (2010) used the same rates of KADoNiS v0.3, as we did in our models. The rate reduction of several *s*-process path bottlenecks, in particular at ^{63}Cu, hinders the *s*-process and reduces the overproduction factors above the copper isotopes, when using the newer rate compilation.

(iv) The $^{12}C(\alpha, \gamma)^{16}O$ rate sources are listed in Table 7. The rate of Kunz et al. (2002) is the lowest and about 10–20 per cent smaller than the NACRE rate in the relevant temperature region for core He-burning. A higher rate means that the star can obtain the same amount of energy at lower temperatures. In this way, a lower rate supports the *s*-process. Tur et al. (2009) studied the impact of the uncertainty in the $^{12}C(\alpha, \gamma)^{16}O$ rate. And a reduction of this rate by 10–20 per cent increases the overproduction factors on average by 0.1–0.2 dex.

(v) Neglecting mass-loss means that the core is larger during the core He-burning phase, and consequently has higher temperatures. The et al. (2007) point out the possible impact of such a change with their models 25N and 25NM. Pignatari et al. (2010) and Raiteri et al.

(1991a) used stellar models calculated with the Frascati Raphson Newton Evolutionary Code (FRANEC), which did not include mass-loss (Käppeler et al. 1994). The maximal core size of their model during He-burning is $M_{\rm He}^{\rm max} = 6.17\,{\rm M}_{\odot}$ (Pignatari, private communication). It lies thus between the core sizes of our models A25s0 and A25s4 (see Table 2). The mass-loss introduces therefore a rather moderate uncertainty, but still reduces the overproduction factors, $n_{\rm c}$ and $\langle\tau\rangle$, by about 10 per cent.

These various differences in the nuclear reaction input as well as the stellar models make it difficult to disentangle the impact of the different parameters quantitatively. On the qualitative side, our models are consistent with the previous publications considering the differences discussed above.

If we compare the difference between our two models (A25s0, A25s4) and the other model, we can also conclude that the effect of rotation at solar metallicity is rather moderate and well within the nuclear reaction rate uncertainties. This is the case because ^{22}Ne production by rotation-induced mixing does not play a role at $Z = {\rm Z}_{\odot}$. As discussed above, the rotation still leads to a stronger production at solar metallicity. The impact of rotation becomes stronger and stronger as the initial metallicity decreases.

Recently, Chieffi & Limongi (2015) presented preliminary results where their models for fast-rotating massive stars at low metallicity can efficiently produce elements also up to Pb. In their models, the *s*-process production is due to the mixing of ^{13}C into the helium core, which provides additional neutrons. A comparison is not possible at this stage since the models are not described in details in that study.

6.2 Comparison to observations

6.2.1 Production of elements at the Sr and Ba peaks

Spectroscopic observations have shown a secondary trend of [Cu/Fe] (e.g. Bisterzo et al. 2005; Sobeck et al. 2008, and references therein), in agreement with *s*-process calculations which predicts that a major part of Cu comes from the *s*-process in massive stars (e.g. Pignatari et al. 2010). The same trend is expected for Ga, for which only few observations and upper limits are available from low-metallicity stars and not a real comparison can be made, and for Ge (see discussion in Pignatari et al. 2010). More data are available for Ge compared to Ga (Cowan et al. 2005), but the metallicity range of interest is still not fully covered by observations. As mentioned before, we show that rotation would not change the secondary nature of the *s*-process production of these elements.

Travaglio et al. (2004) compared the spectroscopic observations of the Sr-peak elements Sr, Y and Zr at different metallicities with the *s*-process distribution in the Solar system obtained from GCE calculations. They proposed that a lighter element primary process (or LEPP) was responsible for both the observations and the missing *s*-process abundances in the solar distribution. Later, Montes et al. (2007) compared the 'stellar LEPP' signature at low metallicity with the 'solar LEPP' in the Solar system, concluding that while they are compatible, also explosive nucleosynthesis processes can be responsible for the same elemental signature in the early Galaxy. While the existence of the solar LEPP has been recently questioned (Maiorca et al. 2012; Cristallo et al. 2015), we cannot exclude that an additional *s*-process component is needed to contribute to its total amount. We have seen in this work that it is quite unlikely that the *s*-process in fast-rotating massive stars is the responsible, due to its secondary nature and its significance only at much lower metallicities for elements in the Sr mass region and heavier. On the other hand, Cescutti et al. (2013) and Barbuy et al. (2014) showed that *s*-process in fast-rotating massive stars is compatible with observations at low metallicity (e.g. Hansen et al. 2013). Alternative or complementary theoretical scenarios proposed to explain the stellar LEPP are explosive nucleosynthesis components, mainly associated with neutrino-driven winds on top of the forming neutron star (e.g. Fröhlich et al. 2006; Qian & Wasserburg 2008; Farouqi et al. 2009; Arcones & Montes 2011).

We have seen a scatter in the production up to Ba, which is strongly affected by nuclear uncertainties. Additionally, a scatter in Sr production is intrinsic to the rotation-boosted *s*-process, since a varying rotation rate would lead to a varying amount of primary ^{22}Ne and thus to a varying neutron exposure and *s*-process production, respectively. Typically, the *s*-process in massive stars produces only minor amounts of Ba and [Sr/Ba] is around +2, with an upper limit of $\approx +2.3$. However, due to the seed limitation and the larger neutron capture per iron seed, the enhanced *s*-process in fast-rotating massive stars can produce more significantly also elements at the Ba neutron-magic peak. On the other hand, as shown by Pignatari et al. (2013), the intrinsic nature of ^{22}Ne as a neutron source and neutron poison does not allow one to efficiently feed also heavier elements along the *s*-process path, up to Pb.

6.2.2 The very low Z stars: the case of CEMP-no stars

At metallicities [Fe/H] $\lesssim -2$, it is possible to observe a large number of 'carbon-enhanced metal-poor' (CEMP; [C/Fe] > 0.7; Aoki et al. 2007) stars, which exhibit large excesses of carbon with values of [C/Fe] reaching more than 4.0 dex. At the same time, nitrogen, oxygen and other elements are also largely overabundant. These stars are very old low-mass stars (about $0.8\,{\rm M}_{\odot}$) still surviving and exhibiting the particular nucleosynthetic products of the first stellar generations.

CEMP stars were classified in CEMP-s, CEMP-r/s and CEMP-r (e.g. Beers, Preston & Shectman 1992; Beers & Christlieb 2005), depending on the observed abundances of s-elements (mainly Ba) and r-elements (mainly Eu). Another group was identified the CEMP-no stars, with much weaker overabundances of n-capture elements (typically [Ba/Fe] < 1). Nevertheless, a fraction of them contains measurable amounts of heavy s-elements. Recent catalogues may be found by Masseron et al. (2010), Allen et al. (2012), Bisterzo et al. (2012), Lugaro et al. (2012), Norris et al. (2013), Bonifacio et al. (2015) and Hansen et al. (2015). The CEMP-no stars clearly dominate for low-metallicity stars with [Fe/H] < -3.0. Several of these stars are still main sequence or subgiant objects; thus, their particular abundances are likely not resulting from self-enrichment, but from the nucleosynthetic contributions of previous massive stars, called the source stars, possibly belonging to the first stellar generations.

Many different kinds of models have been suggested to explain the properties of the CEMP-no stars; see a review of these models by Nomoto, Kobayashi & Tominaga (2013). Two kinds of models are presently emerging (Norris et al. 2013): the mixing and fallback models of faint supernovae (Nomoto, Kobayashi & Tominaga 2013; Tominaga, Iwamoto & Nomoto 2014) and the models of spinstars, i.e. of massive stars with fast rotation and mass-loss (Meynet et al. 2006), a combination of both sets of models being also possible. Recently, Maeder, Meynet & Chiappini (2015) have provided many tests showing that the particular CNO abundances of CEMP-no stars result from products of He-burning (mainly C and O) having undergone partial mixing and processing in the H-burning shell before being ejected into the interstellar medium. This result is

Table 8. Strontium and barium abundances for CEMP-no stars with [Sr/Fe] >0.

Star[Ref]	$T_{\rm eff}$	log g	$\left[\frac{\rm Fe}{\rm H}\right]$	$\left[\frac{\rm Sr}{\rm Fe}\right]$	$\left[\frac{\rm Ba}{\rm Fe}\right]$	$\left[\frac{\rm Sr}{\rm Ba}\right]$
BS 16929−005[a]	5229	2.61	−3.34	0.54	− 0.41	0.95
CS 22949−037[a]	4958	1.84	−3.97	0.55	− 0.52	1.07
HE 0100−1622[b]	5400	3.0	−2.93	0.25	< − 1.80	>2.05
HE 0233−0343[b]	6100	3.4	−4.68	0.32	<0.80	> − 0.48
HE 1300−2201[c]	6332	4.64	−2.61	0.28	− 0.04	0.32
HE 1327−2326[a, c, d]	6180	3.70	−5.76	1.04	<1.46	> − 0.42
HE 1330−0354[c]	6257	4.13	−2.29	0.01	− 0.47	0.48
53327-2044-515[a]	5703	4.68	−4.05	1.09	<0.34	>0.75

References: [a]Norris et al. (2013); [b]Hansen et al. (2015); [c]Allen et al. (2012); [d]Frebel et al. (2005).

based on the analysis of the ^{12}C/^{13}C, [C/N] and [O/N] ratios as well as on the study of the elements involved in the Ne–Na and Mg–Al cycles of H-burning, which all show large excesses and a behaviour completely different from that of the α-elements. At the same time, some of these CEMP-no stars show the presence of s-elements. As shown by the models presented in the previous sections, the mixing processes, by successive back-and-forth motions between the He- and H-burning regions, may also lead to the ^{22}Ne(α,n)^{25}Mg reaction which produces s-elements by neutron captures on seed heavy elements.

The present models show a great sensitivity to both metallicity and rotation of the ratio of s-elements of the first peak (like Sr) to s-elements of the second peak (like Ba). Specifically, the models of 25 $M_\odot$ with $Z = 10^{-3}$, corresponding to [Fe/H] = −1.8, without rotation predict a ratio [Sr/Ba] = 0.13, with rotation [Sr/Ba] = 2.12 (see Fig. 7). For the models with $Z = 10^{-5}$ ([Fe/H] = −3.8), the corresponding values are [Sr/Ba] = 0.03 and 1.17, respectively (see Fig. 8). For the models with $Z = 10^{-7}$ ([Fe/H] = −5.8), the ratios become [Sr/Ba] = 0.05 and −0.08 (see Fig. 9). Thus, we notice that for non-rotating models the ratio [Sr/Ba] decreases slightly for lower Z, nevertheless still remaining positive. For rotating models, at [Fe/H] = −1.8, [Sr/Ba] is very high, decreasing first slightly for lower Z and then very steeply, becoming negative at [Fe/H] = −5.8. As shown by the above models, the physical reason of these changes is that at lower Z the many free neutrons produced by (α,n) captures can more easily saturate the less abundant seeds and thus the succession of n-captures may proceed to nuclei of higher atomic masses. According to Section 5.1, the trend with rotation mainly results from the larger cores and thus higher temperatures, which produce higher fractions of burned ^{22}Ne.

In the sample of 46 CEMP-no stars, we may collect from the mentioned catalogues (Maeder et al. 2015), 39 stars have [Sr/Fe] data measured. Their mean value is [Sr/Fe] = −0.36. There are eight CEMP-no stars with a significant excess of the ratio [Sr/Fe], say with [Sr/Fe] > 0. Table 8 shows their [Sr/Fe], [Ba/Fe] and [Sr/Ba] ratios. We see that all stars in the range of [Fe/H] = −2.2 to −4.0 have clearly *positive* values of the [Sr/Ba] ratios, up to more than 2.05. The two stars with the lowest [Fe/H] values, HE 0233−0343 ([Fe/H] = −4.68) and HE 1327−2326 ([Fe/H] = −5.76), both have *negative* values of their lower limits for [Sr/Ba] of −0.48 and −0.42.

There is, for now, only one star known with an [Fe/H] ratio lower than those quoted above, this is SMSS 0313−6708 (Keller et al. 2014). Its chemical abundances are mainly given in the form of upper limits: [Fe/H] = < −7.3, [Sr/H] < −6.7, [Ba/H]<−6.1. We notice that these limits may also support a positive [Sr/Fe] together with a negative [Sr/Ba] ratio for this object with an extremely low metallicity, but, since these are only upper limits, it is not possible at the moment to interpret the heavy element abundances in this star.

Despite the fact that the sample of these most extreme objects is limited, we may note impressive agreement between the model predictions and the observations with the following conclusions.

(i) If we consider both models without and with rotation, the ranges of theoretical and observed [Sr/Ba] ratios correspond very well lying between [Sr/Ba] ∼ −0.5 and +2.0.

(ii) Without the effects of rotation, the predicted range of [Sr/Ba] ratios lies between 0.0 and 0.2, being much shorter than the observed range. Thus, non-rotating models are unable to account for the observed range of [Sr/Ba] (Cescutti et al. 2013).

(iii) The range of [Sr/Ba] ratios predicted by rotating models is much broader extending from −0.5 to 2.1, in agreement with observations. Thus, rotating models are needed for accounting the abundances of s-elements in very low metallicity stars, as shown in the last reference.

(iv) Not only the observed range is correctly predicted by the models, but also the observed trend of lower [Sr/Ba] for stars with the lower [Fe/H] ratios.

We note that this last effect is quite consistent with the so-called 'Ba-floor' recently found by Hansen et al. (2015). This is a plateau in the absolute Ba abundances of CEMP stars for stars with [Fe/H] < −3.0. Indeed, the existence of this Ba-floor implies that for the lower [Fe/H] ratios the observed [Ba/Fe] ratios become larger, and thus [Sr/Ba] lower as shown by the present models.

This confirms the many pieces of evidence (Maeder et al. 2015) consistent with a significant role of rotation in stars of low metallicities, an effect with a high impact on the early chemical and spectral evolution of galaxies.

7 CONCLUSIONS

We calculated a large grid of rotating massive star models to determine the impact of rotation on slow neutron captures from solar down to very low metallicities following our previous exploratory studies. The main results of this study are the following.

(i) Our models show that rotation not only enables the production of primary nitrogen, but also of important quantities of primary ^{22}Ne at all metallicities. Whereas the neutron source for the *s*-process in non-rotating models is secondary, the neutron source is primary in rotating models.

(ii) At solar metallicity, rotation-induced mixing increases the weak *s*-process production but its impact is modest (within a factor of 2) and the production in rotating models stops at the strontium peak as in standard models.

(iii) As the metallicity decreases, the amount of iron seeds decreases and the iron seeds are the main limitation to the production of heavier elements in rotating models, in which the neutron source is primary. The decreasing amount of seeds does not prevent the production of heavier elements though. On the other hand, the lack of seeds means that not only the seeds get depleted but elements in the mass range A = 60–80 also get depleted as the production peak shifts to the strontium peak by $Z = 10^{-3}$ and elements up to the barium peak are efficiently produced at that metallicity and very low metallicities. The final [Sr/Ba] ratio that we obtain is covering the range between roughly −0.5 and 2.1.

(iv) The strong dependence of production of the barium peak on metallicity and initial rotation rate means that our models provide a

natural explanation for the observed scatter for the [Sr/Ba] ratio at the low metallicities.

(v) The general decrease with metallicity of the [Sr/Ba] ratio in our models also matches the decreasing ratio observed in the small current sample of CEMP-no stars at extremely low [Fe/H].

(vi) Although they are challenging to measure, isotopic ratios, for example for magnesium isotopes, have a great potential for constraining stellar models.

There are important uncertainties that affect the results presented in this paper. On the nuclear side, the dominant uncertainties are the exit channel ratios between n and γ for α-captures on ^{17}O and ^{22}Ne. The first ratio determines whether ^{16}O is a strong neutron poison or only a strong absorber, while the second determines the strength of the neutron source ^{22}Ne(α, n). On the stellar side, the interplay of mean molecular weight and magnetic fields with rotation-induced instabilities and mixing is the main uncertainty. Concerning the stabilizing effect of mean molecular weight on shear mixing, we have used a conservative prescription for shear mixing. It is not fully clear yet whether magnetic fields would increase or decrease rotation-induced mixing. If we compare models computed with the Tayler–Spruit dynamo and models without, we observed that starting from the same initial conditions (mass, metallicity, rotation), models with the Tayler–Spruit dynamo are more mixed (see for instance Maeder & Meynet 2005). On the other hand, this does not imply that the models with the Tayler–Spruit dynamo would produce more primary ^{14}N and ^{22}Ne. Primary nitrogen production needs strong enough mixing in a very specific region of the star, i.e. between the helium core and the hydrogen burning shell. Whether this mixing will be strong enough depends on the gradients of the angular velocity and of the mean molecular weight in this region, as explained above in this paper (see also Meynet et al. 2013).

These uncertainties affect quantitatively the results obtained in this study and new models will be required, e.g. when updated reaction rates become available. Nevertheless, the results will remain true qualitatively and their ability to explain many observed abundance features provides a strong support for the impact of rotation-induced mixing at low metallicities.

ACKNOWLEDGEMENTS

The research leading to these results has received funding from the European Research Council under the European Union's Seventh Framework Programme (FP/2007-2013)/ERC Grant Agreement no. 306901. RH acknowledges support from the World Premier International Research Center Initiative (WPI Initiative), MEXT, Japan and from the Eurogenesis EUROCORE programme. MP thanks the support from the 'Lendület-2014' Programme of the Hungarian Academy of Sciences (Hungary) and from SNF (Switzerland). This work was partially supported by the European Research Council GA 321263-FISH and the UK Science and Technology Facilities Council (grant ST/M000958/1).

REFERENCES

Allen D. M., Ryan S. G., Rossi S., Beers T. C., Tsangarides S. A., 2012, A&A, 548, A34
Anders E., Grevesse N., 1989, Geochim. Cosmochim. Acta, 53, 197
Angulo C. et al., 1999, Nucl. Phys. A, 656, 3
Aoki W., Beers T. C., Christlieb N., Norris J. E., Ryan S. G., Tsangarides S., 2007, ApJ, 655, 492
Arcones A., Montes F., 2011, ApJ, 731, 5
Asplund M., Grevesse N., Sauval A. J., 2005, in Barnes T. G., III, Bash F. N., eds, ASP Conf. Ser. Vol. 336, Cosmic Abundances as Records of Stellar Evolution and Nucleosynthesis. Astron. Soc. Pac., San Francisco, p. 25
Baraffe I., Takahashi K., 1993, A&A, 280, 476
Baraffe I., El Eid M. F., Prantzos N., 1992, A&A, 258, 357
Barbuy B., Zoccali M., Ortolani S., Hill V., Minniti D., Bica E., Renzini A., Gómez A., 2009, A&A, 507, 405
Barbuy B. et al., 2014, A&A, 570, A76
Beer H., Voss F., Winters R. R., 1992, ApJS, 80, 403
Beers T. C., Christlieb N., 2005, ARA&A, 43, 531
Beers T. C., Preston G. W., Shectman S. A., 1992, AJ, 103, 1987
Bennett M. E. et al., 2012, MNRAS, 420, 3047
Best A. et al., 2011, Phys. Rev. C, 83, 052802
Best A. et al., 2013, Phys. Rev. C, 87, 045805
Bisterzo S., Pompeia L., Gallino R., Pignatari M., Cunha K., Heger A., Smith V., 2005, Nucl. Phys. A, 758, 284
Bisterzo S., Gallino R., Straniero O., Cristallo S., Käppeler F., 2012, MNRAS, 422, 849
Bisterzo S. et al., 2015, MNRAS, 449, 506
Blake J. B., Schramm D. N., 1976, ApJ, 209, 846
Blake J. B., Woosley S. E., Weaver T. A., Schramm D. N., 1981, ApJ, 248, 315
Bonifacio P. et al., 2015, A&A, 579, A28
Caughlan G. R., Fowler W. A., 1988, At. Data Nucl. Data Tables, 40, 283 (CF88)
Caughlan G. R., Fowler W. A., Harris M. J., Zimmerman B. A., 1985, At. Data Nucl. Data Tables, 32, 197
Cescutti G., Chiappini C., Hirschi R., Meynet G., Frischknecht U., 2013, A&A, 553, A51
Cescutti G., Romano D., Matteucci F., Chiappini C., Hirschi R., 2015, A&A, 577, A139
Chiappini C., Hirschi R., Meynet G., Ekström S., Maeder A., Matteucci F., 2006, A&A, 449, L27
Chiappini C., Frischknecht U., Meynet G., Hirschi R., Barbuy B., Pignatari M., Decressin T., Maeder A., 2011, Nature, 472, 454
Chieffi A., Limongi M., 2013, ApJ, 764, 21
Chieffi A., Limongi M., 2015, in Meynet G., Georgy C., Groh J., Stee P., eds, Proc. IAU Symp. 307, New Windows on Massive Stars: Asteroseismology, Interferometry, and Spectropolarimetry. Cambridge Univ. Press, Cambridge, p. 1
Cowan J. J. et al., 2005, ApJ, 627, 238
Cristallo S., Abia C., Straniero O., Piersanti L., 2015, ApJ, 801, 53
Cunha K., Hubeny I., Lanz T., 2006, ApJ, 647, L143
Descouvemont P., 1993, Phys. Rev. C, 48, 2746
Dillmann I., Heil M., Käppeler F., Plag R., Rauscher T., Thielemann F.-K., 2006, in Woehr A., Aprahamian A., eds, AIP Conf. Ser. Vol. 819, Capture Gamma-Ray Spectroscopy and Related Topics. Am. Inst. Phys., New York, p. 123
Dufton P. L. et al., 2006, A&A, 457, 265
Eggenberger P., Meynet G., Maeder A., Hirschi R., Charbonnel C., Talon S., Ekström S., 2008, Ap&SS, 316, 43
Ekström S., Meynet G., Chiappini C., Hirschi R., Maeder A., 2008, A&A, 489, 685
El Eid M. F., Meyer B. S., The L.-S., 2004, ApJ, 611, 452
Farouqi K., Kratz K.-L., Mashonkina L. I., Pfeiffer B., Cowan J. J., Thielemann F.-K., Truran J. W., 2009, ApJ, 694, L49
Frebel A. et al., 2005, in Hill V., Francois P., Primas F., eds, Proc. IAU Symp. 228, From Lithium to Uranium: Elemental Tracers of Early Cosmic Evolution. Cambridge Univ. Press, Cambridge, p. 207
Frischknecht U., 2012, PhD thesis, Univ. Basel
Frischknecht U., Hirschi R., Thielemann F.-K., 2012, A&A, 538, L2
Fröhlich C., Martínez-Pinedo G., Liebendörfer M., Thielemann F.-K., Bravo E., Hix W. R., Langanke K., Zinner N. T., 2006, Phys. Rev. Lett., 96, 142502
Fynbo H. O. U., Diget C. A., Bergmann U. C., ISOLDE Collaboration, 2005, Nature, 433, 136
Hansen C. J., Bergemann M., Cescutti G., François P., Arcones A., Karakas A. I., Lind K., Chiappini C., 2013, A&A, 551, A57

Hansen T. et al., 2015, ApJ, 807, 173
Heger A., Langer N., 2000, ApJ, 544, 1016
Heger A., Woosley S. E., 2010, ApJ, 724, 341
Heger A., Fryer C. L., Woosley S. E., Langer N., Hartmann D. H., 2003, ApJ, 591, 288
Heger A., Woosley S. E., Spruit H. C., 2005, ApJ, 626, 350
Hirschi R., 2007, A&A, 461, 571
Hirschi R., Meynet G., Maeder A., 2004, A&A, 425, 649
Hirschi R., Frischknecht U., Thielemann F., Pignatari M., Chiappini C., Ekström S., Meynet G., Maeder A., 2008, in Hunt L. K., Madden S., Schneider R., eds, Proc. IAU Symp. 255, Low-Metallicity Star Formation: From the First Stars to Dwarf Galaxies. Cambridge Univ. Press, Cambridge, p. 297
Hunter I., Lennon D. J., Dufton P. L., Trundle C., Simón-Díaz S., Smartt S. J., Ryans R. S. I., Evans C. J., 2008, A&A, 479, 541
Hunter I. et al., 2009, A&A, 496, 841
Iliadis C., Longland R., Champagne A. E., Coc A., Fitzgerald R., 2010, Nucl. Phys. A, 841, 31
Imbriani G., Limongi M., Gialanella L., Terrasi F., Straniero O., Chieffi A., 2001, ApJ, 558, 903
Jaeger M., Kunz R., Mayer A., Hammer J. W., Staudt G., Kratz K. L., Pfeiffer B., 2001, Phys. Rev. Lett., 87, 202501
Janka H.-T., 2012, Annu. Rev. Nucl. Part. Sci., 62, 407
Käppeler F., Gallino R., Busso M., Picchio G., Raiteri C. M., 1990, ApJ, 354, 630
Käppeler F. et al., 1994, ApJ, 437, 396
Käppeler F., Gallino R., Bisterzo S., Aoki W., 2011, Rev. Mod. Phys., 83, 157
Karakas A. I., Lugaro M. A., Wiescher M., Görres J., Ugalde C., 2006, ApJ, 643, 471
Keller S. C. et al., 2014, Nature, 506, 463
Kobayashi C., Umeda H., Nomoto K., Tominaga N., Ohkubo T., 2006, ApJ, 653, 1145
Kunz R., Fey M., Jaeger M., Mayer A., Hammer J. W., Staudt G., Harissopulos S., Paradellis T., 2002, ApJ, 567, 643
Langer N., Arcoragi J.-P., Arnould M., 1989, A&A, 210, 187
Limongi M., Straniero O., Chieffi A., 2000, ApJS, 129, 625
Lodders K., 2003, ApJ, 591, 1220
Longland R., Iliadis C., Karakas A. I., 2012, Phys. Rev. C, 85, 060000
Lugaro M., Karakas A. I., Stancliffe R. J., Rijs C., 2012, ApJ, 747, 2
Maeder A., 1992, A&A, 264, 105
Maeder A., 1997, A&A, 321, 134
Maeder A., Meynet G., 2005, A&A, 440, 1041
Maeder A., Grebel E. K., Mermilliod J.-C., 1999, A&A, 346, 459
Maeder A., Meynet G., Chiappini C., 2015, A&A, 576, A56
Maiorca E., Magrini L., Busso M., Randich S., Palmerini S., Trippella O., 2012, ApJ, 747, 53
Martayan C., Floquet M., Hubert A. M., Gutiérrez-Soto J., Fabregat J., Neiner C., Mekkas M., 2007, A&A, 472, 577
Masseron T., Johnson J. A., Plez B., van Eck S., Primas F., Goriely S., Jorissen A., 2010, A&A, 509, A93
Meyer B. S., Clayton D. D., The L.-S., 2000, ApJ, 540, L49
Meynet G., Maeder A., 2002a, A&A, 381, L25
Meynet G., Maeder A., 2002b, A&A, 390, 561
Meynet G., Ekström S., Maeder A., 2006, A&A, 447, 623
Meynet G., Ekstrom S., Maeder A., Eggenberger P., Saio H., Chomienne V., Haemmerlé L., 2013, in Goupil M., Belkacem K., Neiner C., Lignières F., Green J. J., eds, Lecture Notes in Physics, Vol. 865, Studying Stellar Rotation and Convection. Springer-Verlag, Berlin, p. 3
Montes F. et al., 2007, ApJ, 671, 1685
Ness M., Asplund M., Casey A. R., 2014, MNRAS, 445, 2994
Nishimura N. et al., 2014, in Jeong S., Imai N., Miyatake H., Kajino T., eds, AIP Conf. Ser. Vol. 1594, Origin of Matter and Evolution of Galaxies 2013. Am. Inst. Phys., New York, p. 146
Nomoto K., Kobayashi C., Tominaga N., 2013, ARA&A, 51, 457
Norris J. E. et al., 2013, ApJ, 762, 28
Pignatari M., Gallino R., 2008, in O'Shea B. W., Heger A., eds, AIP Conf. Ser. Vol. 990, First Stars III. Am. Inst. Phys., New York, p. 336
Pignatari M., Gallino R., Meynet G., Hirschi R., Herwig F., Wiescher M., 2008, ApJ, 687, L95
Pignatari M., Gallino R., Heil M., Wiescher M., Käppeler F., Herwig F., Bisterzo S., 2010, ApJ, 710, 1557
Pignatari M. et al., 2013, ApJ, 762, 31
Prantzos N., Hashimoto M., Nomoto K., 1990, A&A, 234, 211
Pumo M. L., Contino G., Bonanno A., Zappalà R. A., 2010, A&A, 524, A45
Qian Y., Wasserburg G. J., 2008, ApJ, 687, 272
Raiteri C. M., Busso M., Picchio G., Gallino R., Pulone L., 1991a, ApJ, 367, 228
Raiteri C. M., Busso M., Picchio G., Gallino R., 1991b, ApJ, 371, 665
Raiteri C. M., Gallino R., Busso M., 1992, ApJ, 387, 263
Rauscher T., Thielemann F.-K., 2000, At. Data Nucl. Data Tables, 75, 1
Rauscher T., Heger A., Hoffman R. D., Woosley S. E., 2002, ApJ, 576, 323
Rayet M., Hashimoto M., 2000, A&A, 354, 740
Reddy B. E., Lambert D. L., Allende Prieto C., 2006, MNRAS, 367, 1329
Sobeck J. S., Primas F., Sneden C., Ivans I. I., 2008, in O'Shea B. W., Heger A., eds, AIP Conf. Ser. Vol. 990, First Stars III. Am. Inst. Phys., New York, p. 187
Spite M. et al., 2005, A&A, 430, 655
Stacy A., Bromm V., Loeb A., 2011, MNRAS, p. 142
Taggart M. et al., 2011, Proc. Science, The first direct measurement of $^{17}O(\alpha,\gamma)^{21}Ne$ and its impact upon *s*-process abundances. SISSA, Trieste, PoS#(NIC XI) 045
Takahashi K., Yokoi K., 1987, At. Data Nucl. Data Tables, 36, 375
Talon S., Zahn J.-P., 1997, A&A, 317, 749
The L.-S., El Eid M. F., Meyer B. S., 2000, ApJ, 533, 998
The L.-S., El Eid M. F., Meyer B. S., 2007, ApJ, 655, 1058
Thielemann F., Arnould M., Hillebrandt W., 1979, A&A, 74, 175
Thielemann F., Nomoto K., Hashimoto M., 1996, ApJ, 460, 408
Tominaga N., Iwamoto N., Nomoto K., 2014, ApJ, 785, 98
Travaglio C., Gallino R., Arnone E., Cowan J., Jordan F., Sneden C., 2004, ApJ, 601, 864
Truran J. W., Cowan J. J., Cameron A. G. W., 1978, ApJ, 222, L63
Tur C., Heger A., Austin S. M., 2009, ApJ, 702, 1068
Wiescher M., Käppeler F., Langanke K., 2012, ARA&A, 50, 165
Woosley S. E., Heger A., Weaver T. A., 2002, Rev. Mod. Phys., 74, 1015
Yoon S.-C., Langer N., Norman C., 2006, A&A, 460, 199
Zahn J. P., 1992, A&A, 265, 115
Zinner E., 2014, in Davis A. M., ed., Treatise on Geochemistry, 2nd edn. Vol. 1, Meteorites and Cosmochemical Processes. Elsevier, Oxford, p. 181

This paper has been typeset from a TEX/LATEX file prepared by the author.